A PLANAR PROBE DOUBLE LADDER WAVEGUIDE FOR POWER COMBINING AND DIVIDING

By

Mohammed Adil Oudrhiri

A thesis submitted in partial fulfillment of the

requirements for the degree

of

Master of Science

in

Electrical Engineering

Montana State University
Bozeman, Montana
April, 2004

APPPOVAL

of a thesis submitted by

Mohammed Adil Oudrhiri

This thesis has been read by each member of the thesis committee and has been found to be satisfactory regarding content, English usage, format, citation, bibliographic style, and consistency, and is ready for submission to the college of Graduate Studies.

Jim Becker

Approved for the Department of Electrical & Computer Engineering

Jim Peterson

Approved for the College of Graduate Studies

Bruce McLeod

STATEMENT OF PERMISSION OF USE

In presenting this thesis in partial fulfillment of the requirements for a master's degree at Montana State University, I agree that the library shall make it available to borrowers under the rules of the library.

If I have indicated my intention to copyright this thesis by including a copyright notice page, copying is allowable only for scholarly purposes, consistent with "fair use" as prescribed in the U.S. Copyright Law. Requests for permission for extended quotation from or reproduction of this thesis in whole or in parts may be granted only by the copyright holder.

Mohammed Adil Oudrhiri

April 19, 2004

ACKNOWLEDGEMENT

Thank you to Dr Jim Becker for the opportunity he gave me to research a topic that I find interesting and challenging. His advices were very valuable for the success of this project and to my academic curriculum here in Montana State University. Thank you to Dr Joe Shaw and Dr David Dickensheets for valuable advice and suggestions concerning my thesis and also for serving as members of my graduate committee. I also appreciate the work of Paul Rhodes in machining the waveguide.

I could never have completed this project without the blessing of God. Special thanks to my parents, Said and Chafica Oudrhiri.

TABLE OF CONTENTS

TABLE OF CONTENTS-CONTINUED

LIST OF TABLES

Table Page

LIST OF FIGURES

Figure Page

LIST OF FIGURES

Figure Page

5.9 Contour plot of the combiner /divider 70

5.10 Photograph of the bottom half of the double ladder divider / combiner....72

5.11 The S parameters of the machined waveguide 73

ABSTRACT

This thesis presents an initial investigation of a planar probe double ladder power combiner / divider. The structure is analogous to the coaxial double ladder of Sanada, Fukui and Nogi*. The planar probe structure utilizes a series of planar transmission lines and probes to inject or receive power which is combined or divided inside a rectangular waveguide cavity. The structure was developed in a manner for its eventual implementation at W-band (75.0-110.0 GHz) frequencies and above using proven micromachining techniques. A combination of analytical modeling, transmission line analysis and full wave simulations are used to design a four-way power combiner / divider for operation in R-band (1.7-2.6 GHz). The structure was realized using classical machining and exhibited a –15 dB return loss of 23% and a 0.5 dB return loss (with respect to the standard –6 dB level of a 4-way divider) of 26%. The results of this research lay the foundation for a broad-based examination of micromachined power combining / dividing structures for millimeter and submillimeter wave applications.

CHAPTER ONE

INTRODUCTION

High-power, low-cost sources spanning from radio frequencies to millimeter wave frequencies are required for many applications such as imaging radars, satellite communication broadcasting and remote sensing. For this reason, the demand for solid-state local oscillators has been increasing rapidly. The current interest in potential applications for the spectrum from 100 GHz to 1 THz has also fostered a strong need for sub-millimeter-wave receivers, mixers and sources, especially tunable high-power sources.

To meet this need, traveling-wave tubes have traditionally been used. However, tubes are expensive, bulky and require high operating voltages. As an alternative, solid-state devices offer several advantages, such as lower weight, smaller size, wider bandwidths, and lower operating voltages. Some current examples of solid state-devices providing usable power above 100 GHz include Indium Phosphide (InP) high electron mobility transistor (HEMT) oscillators producing 0.2 mW at 130.7 GHz [1], Gallium Arsenide (GaAs) tunnel injection transit-time (TUNNETT) diodes producing 100 mW at 107 GHz and 10 mW at 202 GHz [2], and InP Gunn diodes producing 130 mW, 80 mW, and 1 mW at 132 GHz, 152 GHz and 315 GHz respectively [1]. For applications in which more power is required than is available from a single solid-state device, some means of power combining must be employed.

At microwave and millimeter frequencies, many power combining techniques have been invented and tested to provide means to develop sources with high output power. Figure 1.1 shows the various categories found in the domain of combining power [3], and include chip-level, circuit-level and spatial techniques.

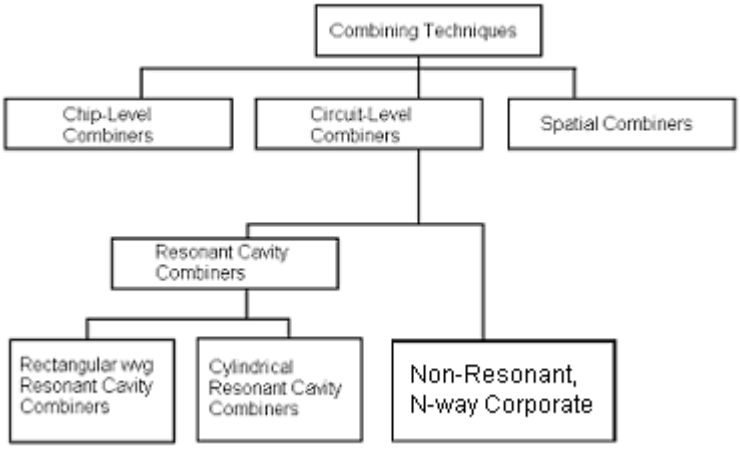

Figure1.1 Various techniques for combining power.

For the past twenty years, the use of waveguides as a tool to combine and split power at microwave frequencies has been investigated. Waveguides have several advantages over two-wire, coaxial and planar transmission lines. For example, dielectric losses are lower in waveguides than in typical transmission lines. The insulating dielectric material that exists in a given transmission line behaves as the dielectric of a capacitor. If an electric field appears across the two poles, it will cause a heating of the dielectric and results in a power loss. The dielectric present in waveguides is typically air, yielding much lower dielectric

loss. The dielectric material that provides mechanical support to a given transmission line is responsible for the transmission line's dielectric loss. It is interesting to note that in recent years considerable research has been devoted to reduce dielectric loss in planar transmission lines. Most of these investigations focus on removing unwanted dielectric material through micromachining and/or supporting one of the conductors on a micron thin membrane.

Another important advantage of waveguides is their higher power handling capability over classical transmission lines. For example, waveguides can take more power than coaxial lines of the same size because power-handling capability is directly related to the distance between conductors. Yet another advantage of waveguides is their ability to transition smoothly into high-gain horn antennas. Such an advantage has been put to significant use in submillimeter-wave remote sensing. Finally, a variety of post-fabrication tuning is available when utilizing waveguide-based circuitry.

Hollow metal waveguides, however, have some disadvantages too. Physical size is the primary lower-frequency limitation; for example, a rectangular waveguide if used at 1 MHz would measure about 150 meters in width. Physical size is likewise a high-frequency limitation for conventional waveguides. As frequency increases, waveguide dimensions must follow the shrinking wavelength. Conventional machining of such waveguides

becomes expensive when the dimensions begin to be best described in fractions of millimeter instead of in millimeters, centimeters or inches. For example, a WR-5 waveguide (140-220 GHz) has cross-sectional dimensions of 1.30 mm by 0.648mm. Conventional machining of such a guide to tight dimensional tolerance is costly. In the last decade significant advances have been made in realizing such waveguides using various micromachining techniques. Recent demonstrations of efficient coupling between micromachined waveguides and planar circuitry suggest the potential for low-cost realization of submillimeter-wave circuitry that includes both planar and waveguide elements. For example, a silicon micromachined diamond-shaped waveguide fed by Finite Ground Coplanar (FGC) transmission lines [4] was designed and assembled to operate at W-band[1]. In other reported work [5], a freestanding printed E-plane probe has been demonstrated, suggesting that such a transition is scalable to submillimeter-wave frequencies

In this thesis, a microwave model of a power-combining structure that is scalable to submillimeter-wave frequencies using previously demonstrated micromachining techniques will be investigated. Such a structure is attractive in that it couples the advantages of waveguide with the wealth of options afforded by planar circuitry, all realizable in a low-cost batch fabrication process.

Toward this end, a detailed evaluation of work presented on the coaxial "double ladder power combiner/divider" [6] will be pursued. Conditions for perfect power combining and dividing in such a structure will be derived. A commercially available

[1] W-band frequencies between 75 and 110 GHz.

full-wave field solver (High Frequency Structure Simulator, HFSS from Ansoft) [7] will be used to verify designs found in the literature. A design methodology using HFSS will be developed and then employed in designing a planar version of the double ladder structure. A four-way planar version will be demonstrated numerically using a conventionally machined WR-430 (1.70-2.60 GHZ) split-block waveguide and microstrip feeds. Through implementation with micromachining process, such a structure can be frequency scaled to operate in W-band and above

Thesis Overview

Chapter 2 presents a brief summary of different techniques currently used to combine and divide microwave power. This chapter briefly discuss operation theory and compare advantages and disadvantages of those techniques. The S parameters and applications of each system will be discussed.

Chapter 3 discusses different criteria needed to obtain perfect power dividing and combining for the double ladder structure. Design equations are derived for multiple numbers of inputs. S parameters will be obtained for the system and frequency response in X-band will be examined.

In chapter 4, solutions via the commercial microwave simulator HFSS are obtained for the coaxial double ladder combiner. Several design aspects are verified including bandwidth, efficiency and power splitting ratio.

Chapter 5 presents a design methodology for realizing a planar version of the coaxial double ladder structure. The methodology is demonstrated through an in-depth example of a four-way divider / combiner in R band (1.70-2.60 GHz). Measured results are compared to those predicted through full-wave simulation.

Finally in chapter 6 conclusions are drawn and future work suggested.

CHAPTER TWO

POWER COMBINING ARCHITECTURES

Several power-combining techniques are mentioned in chapter 1 (see Figure 1.1). The various architectures that exist have different advantages and disadvantages. Thus the choice of a given architecture is dependant on the nature of the application.
In this chapter, different power combining architectures are discussed, limitations of each will be pointed out and their performance will be detailed.

Corporate Feed Combiners

Figure 2.1 shows a dividing and combining technique known as the corporate feed architecture. In the figure, an input signal is divided into eight separate signals, amplified, and then reconstructed into a single output. The dividing and combining devices can take several forms; the two most popular are simple T-junctions and Wilkinson structures. Due to their excellent isolation characteristics, Wilkinson devices are generally preferred. Regardless of the dividing/combining device chosen, corporate feed structures suffer from reduced efficiency as the number of devices increases. This technique is thus limited in the number of elements that can be connected together efficiently. It can be seen that as additional elements are added, the lengths of transmission line and the number of nodal combining circuits increases.

The losses in the added lines and combining circuits accumulate and eventually reduce dividing or combining efficiency.

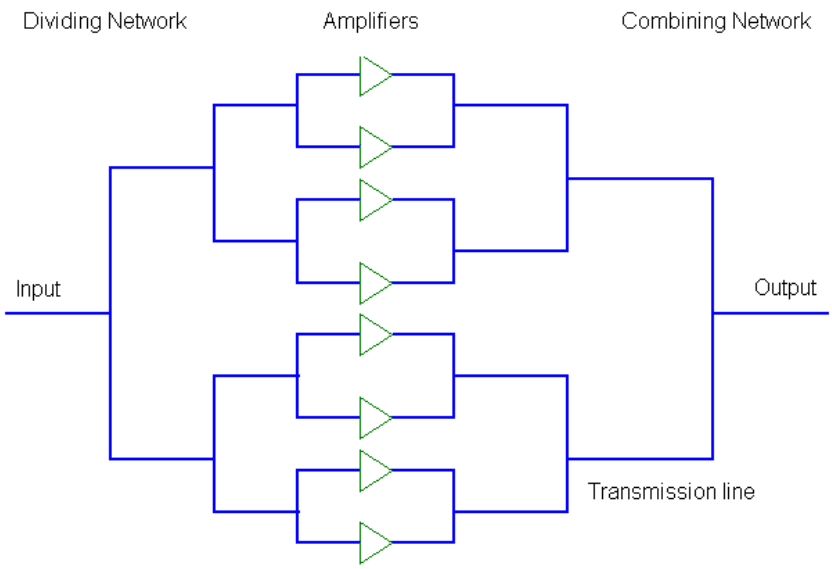

Figure2.1 The Wilkinson power combiner architecture.

An analogy of the transmission line T-junction is available in waveguide. Figure 2.2 shows such a T-junction waveguide. It is not always true that when energy propagating down a waveguide reaches a junction, it simply splits and follows the shape of the structure. Multiple junction types affect the energy flow in different ways.

The T-junction is the most simple of the commonly used waveguide junctions. This structure is divided into two basic types, the E-type and the H-type. The E-type T junction is named so because the junction arm that extends from the main waveguide is in the same direction as the E field.

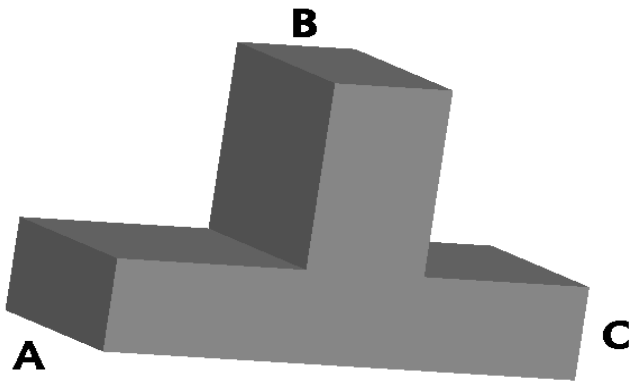

Figure 2.2 The T-junction waveguide.

In the same fashion the name H-type T junction comes from the fact that the long axis of the B arm is parallel to the plane of the magnetic field vector. The way the E-type T-junction works is quite interesting. In Figure 2.3 a, the input is fed into arm B and the outputs are taken at arms A and C. When the electric field propagates between points 1 and 2, point 1 becomes positive and point 2 becomes negative (remember that the electric field vector always points toward the lower potential). The positive charge at point 1 then induces a negative charge on the wall at point 3. The negative charge at point 2 induces a positive charge at point 4. These charges cause the fields to form 180 degrees out of phase in the main waveguide; therefore, the outputs will be 180 degrees out of phase with each other.

In Figure 2.3 b, two in-phase inputs are fed into the junction. The signals at points 1 and 2 have the same phase and amplitude. No difference of potential exists, thus no energy will be coupled out at B. On the other hand, when the two inputs at arms A and C are 180 degrees out of phase, as shown in Figure 2.3 c, points 1 and 2 have a difference of potential, yielding an output at B. This process is similar to the one depicted in Figure 2.3 a.

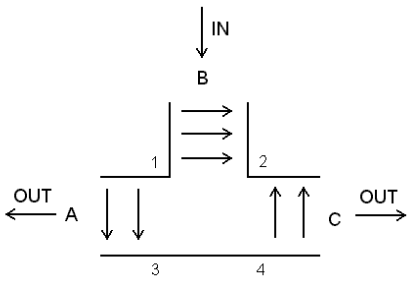

(a) One input, Two Outputs

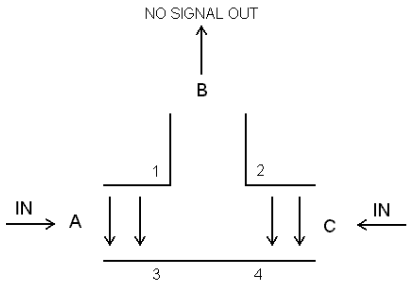

(b) Two inputs, No Output

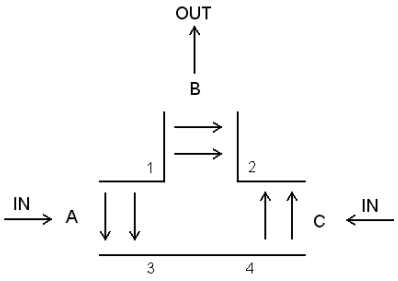

(c) Two inputs, One output.

Figure 2.3 Different ways to couple in and out of an E-type T-junction.

The operation of the H-type T-junction is somewhat different from what we discussed above. In this case the only time we can get power to couple out of an arm is when we have in-phase inputs at the other two arms.

Resonant Cavity Waveguide Combiners

In bulk electronic circuits, a resonant circuit consists of an inductor and a capacitor that are connected together. Reducing the capacitance, the inductance, or both increases the resonant frequency of the circuit. The frequency at which a conventional circuit oscillates is called the resonant frequency. Waveguides can also act as resonant circuits and, since they are hollow, they can be considered as resonant cavities.

A resonant cavity is a space completely enclosed by conducting walls that can contain oscillating electromagnetic fields. The cavity has many advantages and uses at microwave frequencies. For example, resonant cavities can have a very high Q (quality factor) and can be built to handle large amounts of power. The high Q gives these devices a narrow bandpass and allows very precise tuning. Although cavity resonators built for different frequency ranges and applications have a variety of shapes, the basic principles of operation are the same.

The efficiency of power combiners based on waveguide resonant cavities is generally high because the output power of the devices combines directly with low path loss. Such combiners have been demonstrated to frequencies up to 300 GHz [8].

Their down side is that they operate in a narrow bandwidth and do not allow easy mechanical tuning.

Spatial Power Combiners

Figure 2.4 shows another architecture, often referred to as a spatial combiner. The term spatial power combining applies to structures which couple the power in free space. Another common term is quasi-optical power combining which is a subset of spatial power combining. An early spatial combining architecture envisioned arrays of devices coupled to the electromagnetic field, with the RF field spatially controlled by lens and mirror elements, hence the term quasi-optical.

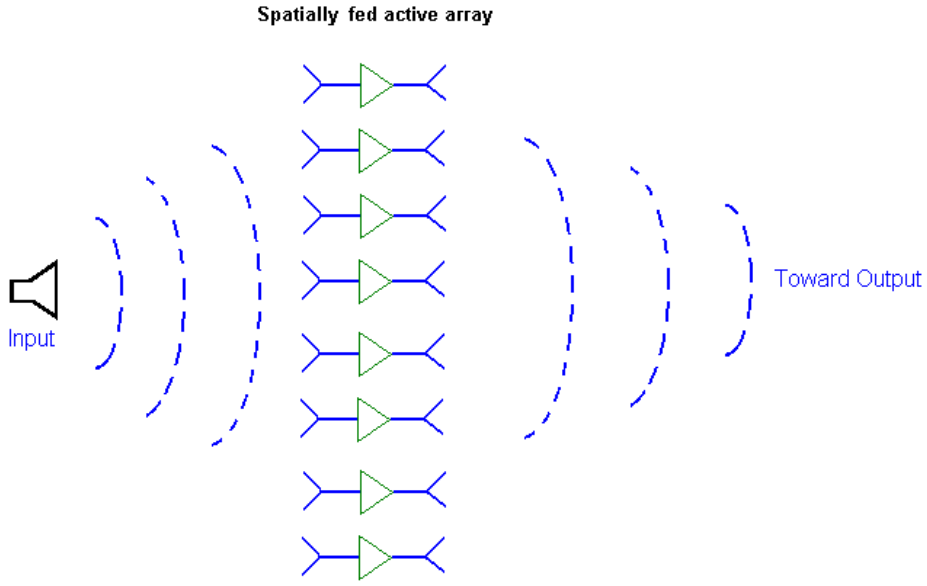

Figure 2.4 A spatial power combiner architecture

Figure 2.5 shows a sketch of an X-band waveguide spatial power combiner system designed at the University of California Santa Barbara. The system has a series of 6-W GaAs Monolithic Microwave Integrated Circuits (MMICs) integrated with slot antenna arrays. Its output power is directly related to the number of MMICs. The system produced up to 120 Watts of output power with 1.9 dB power variations from 8 GHz to 11 GHz. The active array consists of broadband traveling-wave antennas; this architecture improves functionality by circuit integration along the direction of propagation [9]. The combiner was designed to allow only the dominant TE10 mode to propagate, eliminating the problem of higher order modes. Higher power could be achieved by choosing other MMIC amplifier technologies.

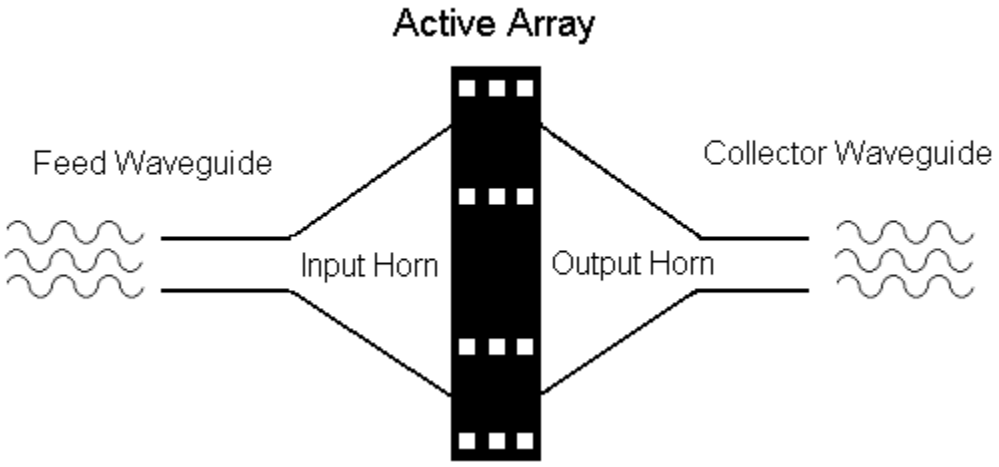

Figure 2.5 X-band Spatial Power Combiner

While the choice between a spatial and a corporate power combiner depends on the nature of the application, ideally the loss behavior of spatial combiners is superior. The loss for a spatial combiner is independent of the number of amplifiers, whereas in the case of a Wilkinson combiner, which is a member of the corporate architecture, the loss is given by

$$total\ loss = (loss\ per\ stage)^k ,$$

where k is the number of stages[10].

Device Failure and Graceful Degradation

The manner in which a power combiner degrades when one or more of its individual sources fail is of significant concern. A combiner whose output power degrades in proportion to the number of individual device failures exhibits graceful degradation.

Quasi-optical combiners utilize arrays of semiconductor devices for power generation and amplification. Degradation in combining efficiency comes from statistical variations in amplifier characteristics like matching and device failure. The behavior of the semiconductor arrays when any device fails is highly important. The advantage of the spatial power combining is that the power produced by the array is obtained by combining the single output amplifier power. In addition, all elements are fed from free space. This allows for lower-cost and lower-power individual elements and graceful degradation. The influence of device failures on power degradation has been

addressed in [11]. Multiple ideas were investigated to improve graceful degradation in combiners, a good discussion of which is cited in [12].

The double Ladder Combiner

The double ladder combiner discussed in this thesis, while waveguide based, is more broadband than a simple resonant cavity device. The double-ladder incorporates circuit-level techniques, but, with simple variations, may include spatial combining techniques as well. Due to its potential for low-cost implementation at frequencies beyond 100 GHz, a planar version of the double ladder is presented.

CHAPTER THREE

THEORY AND DESIGN OF WAVEGUIDE BASED POWER COMBINER AND DIVIDER

Introduction

In this chapter, a waveguide-based power combining and dividing structure will be examined. The structure relies on injecting microwave power inside a waveguide cavity and receiving it at some specific positions. When operating as a divider, the power will start at the central plane of the waveguide and will propagate to be divided, then received at some specific locations as shown in figure 3.1.

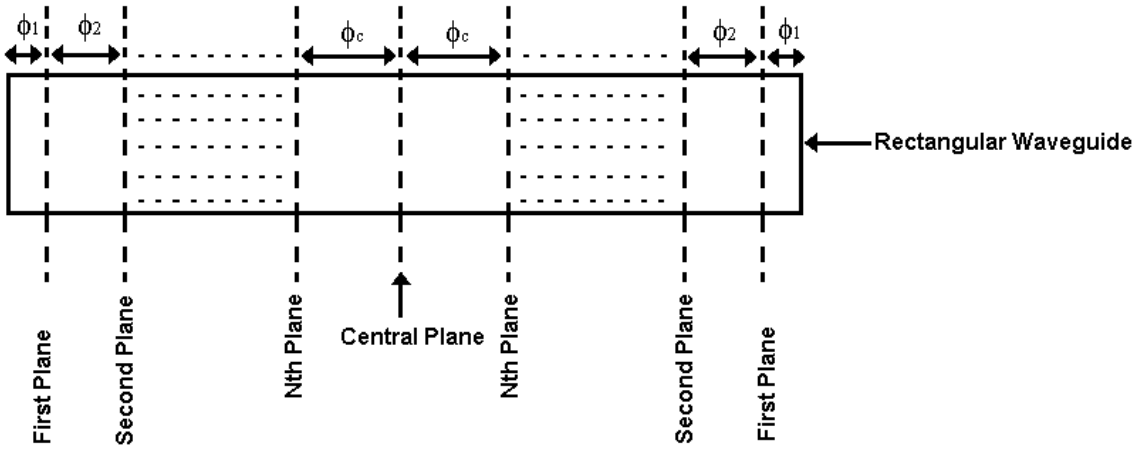

Figure 3.1 Top view of a Rectangular Waveguide.

The dimensions of the system will depend on the frequency of operation and also on the desired performance. The frequency of operation gives the width and the height of the waveguide, e.g. an X band[2] waveguide is 900 mils high and 400 mils wide. The total length of the waveguide is determined by the electrical lengths ϕ_1, ϕ_2, ... ϕ_N and ϕ_c; as is seen from Figure 3.1, we write:

$$waveguide\ length = 2(\sum_{i=1}^{M} \phi_i + \phi_c)$$

where M is the number of planes where the power can be picked up. For example, if we want the input power to be split four ways we will have M=1.

In the rest of the chapter the theory of power propagation and reflection inside the cavity will be discussed. An equivalent circuit will be proposed, and used to obtain design equations necessary to achieve perfect power division. S parameters of the system will be derived so as to compare against measured values. In the next chapters we will investigate two architectures that have the same geometry discussed here; their performance will be compared versus what the theory developed predicts. Conclusions will be drawn and recommendations for future work stated.

Equivalent Half Circuit of the Combiner

Figure 3.2 shows an equivalent circuit of the combiner. The input from the central plane is represented by a current source i_{in} with an admittance y_c given by

[2] X band is the interval between 8.20 GHz and 12.4 GHz.

$$y_c = g_c + jb_c$$

where g_c and b_c represent, respectively, the conductance and susceptance of the probe used to inject the power inside the waveguide.

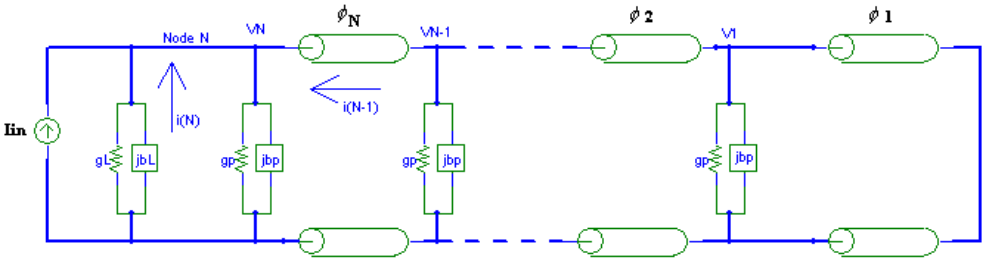

Figure 3.2 Half equivalent circuit of the system.

In Figure 3.2 we can also observe that the locations where power was to be picked up have admittances associated with them as well. In the same fashion as the central probe they are denoted y_p, where

$$y_p = g_p + jb_p$$

All of g_p, b_p, g_L and b_L depend on the type of the probe wanted and are observed to have a frequency dependence, as will be shown in the next chapter. These values will be the essence of what is needed to obtain a desired frequency response. Before we start digging inside the theory of microwave propagation however, an admittance matrix needs to be derived for a simple transmission line. This admittance matrix will be in the form of a two-port network and is used often in the literature for simplicity and convenience. For this purpose consider the transmission line of length L, as shown in Figure 3.3. The system is a simple two-port network for which the impedance matrix will be derived.

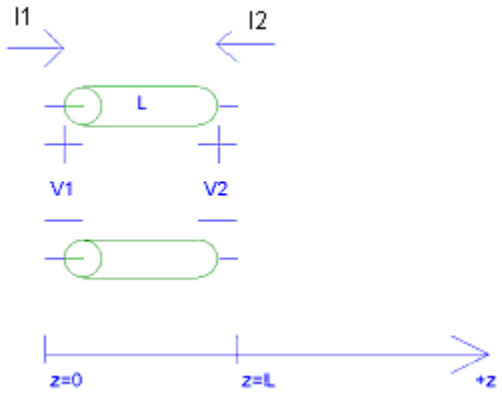

Figure 3.3 The two-port system representing a transmission line of length L.

The impedance equations connecting the voltages and the currents are:

$$V_1 = I_1 Z_{11} + I_2 Z_{12} \tag{3.1}$$

$$V_2 = I_1 Z_{21} + I_2 Z_{22} \tag{3.2}$$

Rewriting the system in matrix form gives the following:

$$\begin{bmatrix} V_1 \\ V_2 \end{bmatrix} = \begin{bmatrix} Z_{11} & Z_{12} \\ Z_{21} & Z_{22} \end{bmatrix} \begin{bmatrix} I_1 \\ I_2 \end{bmatrix} \tag{3.3}$$

The general transmission line equations for the current and the voltage as a function of the distance z are given by (3.4) and (3.5).

$$V(z) = V_o^+ e^{-j\beta z} + V_o^- e^{+j\beta z} \tag{3.4}$$

$$I(z) = \frac{1}{Z_o}(V_o^+ e^{-j\beta z} - V_o^- e^{+j\beta z}) \tag{3.5}$$

In (3.4) and (3.5), the transmission line is assumed to be lossless and is characterized by a phase constant β, V_o^+ and V_o^- are the voltage amplitudes of the incident and reflected waves respectively. Either V_o^+ or V_o^- need to be determined as a function of the other so as to solve equation (3.3).

From equation (3.1) we observe that Z_{11} is given by

$$Z_{11} = \left.\frac{V_1}{I_1}\right|_{I_2=0} \tag{3.6}$$

In figure 3.1 the input is located at z=0. Hence V_1 and I_1 are obtained from the transmission line equations (3.4) and (3.5), thus (3.6) becomes

$$Z_{11} = Z_o \left.\frac{V_o^+ + V_o^-}{V_o^+ - V_o^-}\right|_{I_2=0} \tag{3.7}$$

The restriction imposed by the condition I_2=0 may be used in equation (3.5) at z=L, yielding

$$V_o^- = V_o^+ e^{-2j\beta L} \tag{3.8}$$

Substituting (3.8) into (3.7) gives the following:

$$\begin{aligned} Z_{11} &= Z_o \frac{\mathrm{V_o^+} + \mathrm{V_o^+} e^{-2\,\mathrm{j}\beta\,\mathrm{L}}}{\mathrm{V_o^+} - \mathrm{V_o^+} e^{-2\,\mathrm{j}\beta\,\mathrm{L}}} \\ &= Z_o \frac{1 + e^{-2\,\mathrm{j}\beta\,\mathrm{L}}}{1 - e^{-2\,\mathrm{j}\beta\,\mathrm{L}}} \\ &= Z_o \frac{e^{\mathrm{j}\beta\,\mathrm{L}} + e^{-\,\mathrm{j}\beta\,\mathrm{L}}}{e^{\mathrm{j}\beta\,\mathrm{L}} - e^{-\,\mathrm{j}\beta\,\mathrm{L}}} \\ &= -\mathrm{j} Z_o \frac{e^{\mathrm{j}\beta\,\mathrm{L}} + e^{-\,\mathrm{j}\beta\,\mathrm{L}}}{2} \frac{2\,\mathrm{j}}{e^{\mathrm{j}\beta\,\mathrm{L}} - e^{-\,\mathrm{j}\beta\,\mathrm{L}}} \\ &= -\mathrm{j} Z_o \frac{\cos(\beta\,\mathrm{L})}{\sin(\beta\,\mathrm{L})} \end{aligned}$$

Finally we can write

$$Z_{11} = -\mathrm{j}\,\mathrm{Z_o}\,\mathrm{cotan}(\beta\,\mathrm{L}) \tag{3.9}$$

Proceeding similarly to find Z_{21}, we start with

$$Z_{21} = \left.\frac{\mathrm{V_2}}{\mathrm{I_1}}\right|_{\mathrm{I_2}=0} \tag{3.10}$$

$\mathrm{V_2}$ and $\mathrm{I_1}$ are obtained from the transmission line equations (3.4) and (3.5), and thus (3.10) becomes

$$Z_{21} = Z_o \frac{\mathrm{V_0^+} e^{-\mathrm{j}\beta\,\mathrm{L}} + \mathrm{V_0^-} e^{\mathrm{j}\beta\,\mathrm{L}}}{\mathrm{V_0^+} - \mathrm{V_0^-}} \tag{3.11}$$

Substituting (3.8) into (3.11), we get

$$
\begin{aligned}
Z_{21} &= Z_o \frac{\mathrm{V}_0^+ e^{-\mathrm{j}\beta \mathrm{L}} + \mathrm{V}_0^- e^{\mathrm{j}\beta \mathrm{L}}}{\mathrm{V}_0^+ - \mathrm{V}_0^-} \\
&= Z_o \frac{\mathrm{V}_0^+ e^{-\mathrm{j}\beta \mathrm{L}} + \mathrm{V}_0^+ e^{-2\mathrm{j}\beta \mathrm{L}} e^{\mathrm{j}\beta \mathrm{L}}}{\mathrm{V}_0^+ - \mathrm{V}_0^+ e^{-2\mathrm{j}\beta \mathrm{L}}} \\
&= Z_o \frac{2e^{-\mathrm{j}\beta \mathrm{L}}}{1 - e^{-2\mathrm{j}\beta \mathrm{L}}} \\
&= Z_o \frac{2}{e^{\mathrm{j}\beta \mathrm{L}} - e^{-\mathrm{j}\beta \mathrm{L}}} \\
&= -\mathrm{j} Z_o \frac{1}{\sin(\beta \mathrm{L})}
\end{aligned}
$$

Finally we can write

$$Z_{21} = -\mathrm{j}\, Z_o \mathrm{cosec}(\beta \mathrm{L}) \qquad (3.12)$$

Because of the symmetry of the transmission line, exchanging its input and outputs ends will not alter the values of the impedance coefficients. Hence the normalized impedance matrix represented by equation (3.3) is symmetrical and is given by

$$[z_{ij}] = \begin{bmatrix} -\mathrm{j}\cot(\phi) & -\mathrm{j}\,\mathrm{cosec}(\phi) \\ -\mathrm{j}\,\mathrm{cosec}(\phi) & -\mathrm{j}\cot(\phi) \end{bmatrix} \qquad (3.13)$$

where $\phi = \beta \mathrm{L}$, also known as the electrical length and given in radians.

The normalized admittance can be computed knowing that

$$[y_{ij}] = [z_{ij}]^{-1}$$

Thus we can write

$$[y_{ij}] = \frac{1}{-\cot^2(\phi) + \mathrm{cosec}^2(\phi)} \begin{bmatrix} -\mathrm{j}\cot(\phi) & \mathrm{j}\,\mathrm{cosec}(\phi) \\ \mathrm{j}\,\mathrm{cosec}(\phi) & -\mathrm{j}\cot(\phi) \end{bmatrix}$$

Since

$$-\text{cotan}^2(\phi) + \text{cosec}^2(\phi) = 1,$$

The normalized admittance becomes:

$$\boxed{[y_{ij}] = \begin{bmatrix} -\text{j}\,\text{cotan}(\phi) & \text{j}\,\text{cosec}(\phi) \\ \text{j}\,\text{cosec}(\phi) & -\text{j}\,\text{cotan}(\phi) \end{bmatrix}} \qquad (3.14)$$

With the normalized admittance matrix in hand, the conditions for perfect power division in the waveguide power divider/ combiner will be derived.

Node Equations for the Equivalent Circuit of the Waveguide

In the derivation that follows, it is assumed that each section of transmission line is characterized by an impedance Z_o. Therefore the admittance and impedance matrices, even when unnormalized, will differ only in terms of their electrical lengths (i.e ϕ).

To simplify notation, a given section of transmission line will be represented with the following 2x2 matrix, irrespective of the line's corresponding node location:

$$[y]_{\text{Transmission line}} = \begin{bmatrix} y_{11} & y_{12} \\ y_{21} & y_{22} \end{bmatrix}$$

The values of the admittance matrix elements are given in equation (3.14). Note that the matrix is symmetrical, as mentioned before. The following derivation will be divided into three sections corresponding to the $k = 1, 2 \le k \le N\text{-}1$ and $k = N$ cases. N refers to the number of paired coax probes in the structure.

The First Case k=1

The circuit for k=1 is shown in figure 3.4.

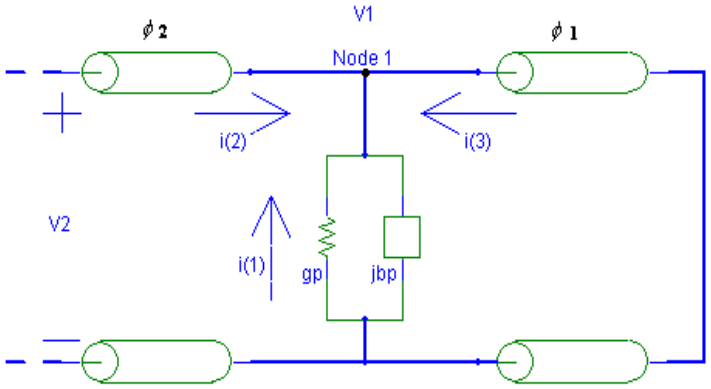

Figure 3.4 Equivalent Circuit for the case k=1.

Writing Kirchoff's Current Law (KCL) at node 1 we get

$$\sum_n i(n) = 0 \Rightarrow i(1) + i(2) + i(3) = 0 \qquad (3.15)$$

Solving for the first current element we get

$$i(1) = -(gp + jbp)\mathrm{V}_1 \qquad (3.16)$$

Matrix (3.14) is used to find i(2) and i(3):

$$i(2) = -y_{11}.\mathrm{V}_1 - y_{12}.\mathrm{V}_2$$

$$i(2) = \mathrm{j}\cot an(\phi_2)\mathrm{V}_1 - \mathrm{j}\,\mathrm{cosec}(\phi_2)\,\mathrm{V}_2 \qquad (3.17)$$

Since the transmission line of electrical length ϕ_1 is shorted, as shown in figure 3.2, we can write

$$i(3) = -y_{11}\mathrm{V}_1 + y_{21}.0$$

Accordingly, we obtain

$$i(3) = \mathrm{j}\cot an(\phi_1)\,\mathrm{V}_1 \qquad (3.18)$$

Putting (3.16), (3.17) and (3.18) in (3.15), we obtain the following equation:

$$[gp + \mathrm{j}(bp - \cot an\phi_2 - \cot an\phi_1)]\mathrm{V}_1 + \mathrm{j}[\mathrm{cosec}\ \phi_2]\,\mathrm{V}_2 = 0 \quad (3.19)$$

Note that V_1 and V_2 are sinusoidal voltages written in phasor form; thus we can write

$$\mathrm{V_k} = \overline{\mathrm{V_k}} e^{\mathrm{j}(\omega_o t + \varphi_k)}$$

where: $\overline{\mathrm{V_k}}$ is the voltage amplitude in volts,

ω_o is the radial frequency and,

φ_k is the phase term in radians.

Replacing the voltage phasors by their expression, equation (3.19) becomes

$$[gp + \mathrm{j}(bp - \cot an\phi_2 - \cot an\phi_1)]\overline{\mathrm{V}_1} e^{\mathrm{j}(\omega_o t + \varphi_1)} + \mathrm{j}[\mathrm{cosec}\phi_2]\,\overline{\mathrm{V}_2} e^{\mathrm{j}(\omega_o t + \varphi_2)} = 0$$

Dividing everything by $e^{\mathrm{j}(\omega_o t + \varphi_1)}$ we obtain

$$\boxed{[gp + \mathrm{j}(bp - \cot an\phi_2 - \cot an\phi_1)]\overline{\mathrm{V}_1} + \mathrm{j}[\mathrm{cosec}\phi_2]\,\overline{\mathrm{V}_2} e^{\mathrm{j}(\varphi_2 - \varphi_1)} = 0} \qquad (3.20)$$

The Second Case $2 \le k \le N-1$

The circuit for $2 \le k \le N-1$ is shown in Figure 3.5.

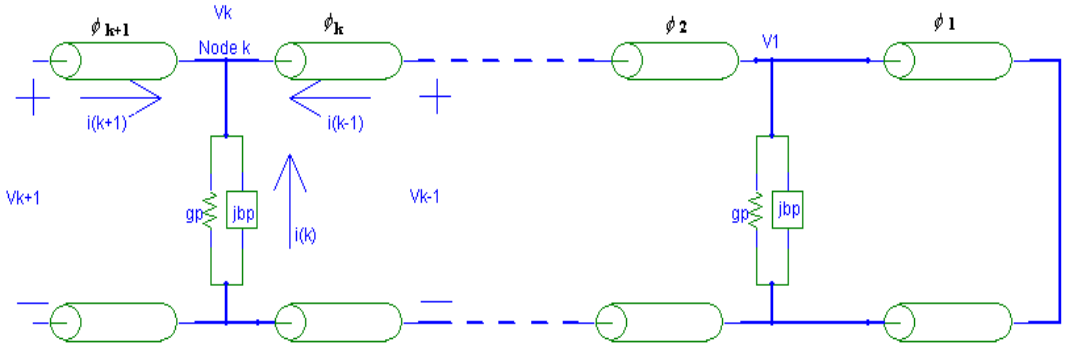

Figure 3.5 Equivalent Circuit for the case $2 \le k \le N-1$.

Writing KCL at node k we get:

$$\sum_n i(n) = 0 \Rightarrow i(k-1) + i(k) + i(k+1) = 0 \tag{3.21}$$

$$i(k) = -(gp + jbp)\, V_k \tag{3.22}$$

$$\begin{aligned} i(k-1) &= -y_{11} V_k - y_{12} V_{k-1} \\ &= j\,\text{cotan}(\phi_k)\, V_k - j\,\text{cosec}(\phi_k)\, V_{k-1} \end{aligned} \tag{3.23}$$

$$\begin{aligned} i(k+1) &= -y_{21} V_{k+1} - y_{22} V_k \\ &= -j\,\text{cosec}(\phi_{k+1})\, V_{k+1} + j\,\text{cotan}(\phi_{k+1})\, V_k \end{aligned} \tag{3.24}$$

Replacing (3.22), (3.23) and (3.24) in (3.21), we obtain

$$j[\text{cosec}\phi_k]\, V_{k-1} + (gp + j\,bp - j\,\text{cotan}\phi_k - j\,\text{cotan}\phi_{k+1}) V_k + j[\text{cosec}\phi_{k+1}] V_{k+1} = 0$$

$$j[\text{cosec}\phi_k]\, \overline{V}_{k-1} e^{j(\omega_o t + \varphi_{k-1})} + (gp + j\,bp - j\,\text{cotan}\phi_k - j\,\text{cotan}\phi_{k+1}) \overline{V}_k e^{j(\omega_o t + \varphi_k)} + j[\text{cosec}\phi_{k+1}] \overline{V}_{k+1} e^{j(\omega_o t + \varphi_{k+1})} = 0$$

Dividing everything by $e^{j(\omega_o t + \varphi_k)}$ we obtain

$$j[\operatorname{cosec}\phi_k]\overline{V}_{k-1}e^{-j(\varphi_k-\varphi_{k-1})}+(gp+jbp-j\operatorname{cotan}\phi_k-j\operatorname{cotan}\phi_{k+1})\overline{V}_k+j[\operatorname{cosec}\phi_{k+1}]\overline{V}_{k+1}e^{j(\varphi_{k+1}-\varphi_k)}=0 \quad (3.25)$$

The Third Case k=N

The equivalent circuit for $k = N$ is shown in Figure 3.6.

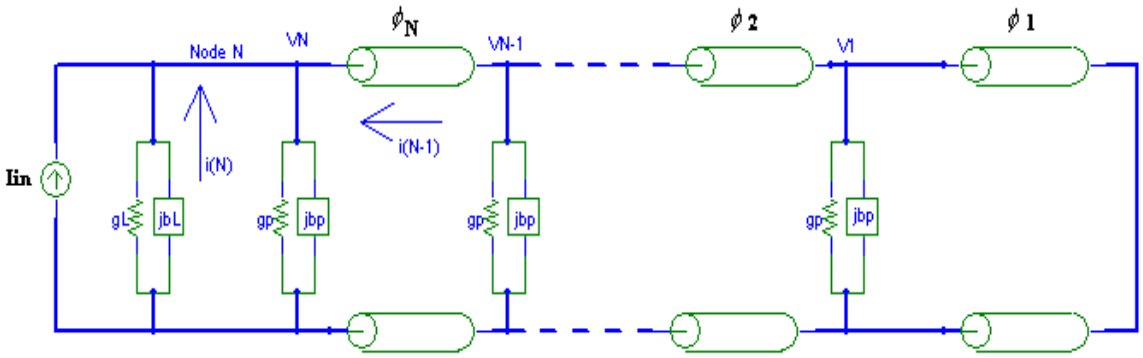

Figure 3.6 Equivalent circuit for the case k=N.

In the circuit of Figure 3.6, i_{in} and the associated admittance g_L and jb_L model the central probe and include the effects of the section of transmission line which separates the central probe from the inner probe pair.

KCL at node N gives

$$\sum_n i(n) = 0 \Rightarrow i(N-1) + i(N) + \frac{i_{in}}{Y_o} = 0 \qquad (3.26)$$

In the above equation the input current from the central probe, i_{in} is normalized to the characteristic admittance of the transmission line to maintain consistency in the use of normalized admittances and admittance matrices.

Writing the currents at the node we get

$$\begin{aligned} i(\mathrm{N}-1) &= -y_{21}V_{N-1} - y_{22}V_N \\ &= -\,\mathrm{j}\,\mathrm{cosec}(\phi_N)\,V_{N-1} + \mathrm{j}\,\mathrm{cotan}(\phi_N)\,V_N \end{aligned} \qquad (3.27)$$

On the other hand

$$i(\mathrm{N}) = -(gp + gL + jbp + jbL)V_N \qquad (3.28)$$

Substituting (3.27) and (3.28) in (3.26), we get

$$Y^{-1}{}_o\, i_{in} - (gp + gL + jbp + jbL)V_N - \mathrm{j}\,\mathrm{cosec}(\phi_N)\,V_{N-1} + \mathrm{j}\,\mathrm{cotan}(\phi_N)\,V_N = 0 \qquad (3.29)$$

Note that i_{in} is a sinusoidal current and can be represented in phasor form as

$$i_{in} = \overline{I_{in}} e^{j(\omega_o t + \psi)} \qquad (3.30)$$

Replacing (3.30) in (3.29) we get

$$Y_o^{-1}\overline{I_{in}} e^{j(\omega_o t + \psi)} - (gp + gL + jbp + jbL)\overline{V_N} e^{j(\omega_o t + \varphi_N)} - \mathrm{j}\,\mathrm{cosec}(\phi_N)\overline{V_{N-1}} e^{j(\omega_o t + \varphi_{N-1})} + \mathrm{j}\,\mathrm{cotan}(\phi_N)\overline{V_N} e^{j(\omega_o t + \varphi_N)} = 0$$

Dividing by $e^{j(\omega_o t + \varphi_N)}$ we get

$$Y_o^{-1}\overline{I_{in}} e^{j(\psi - \varphi_N)} = (gp + gL + jbp + jbL)\overline{V_N} + \mathrm{j}\,\mathrm{cosec}(\phi_N)\overline{V_{N-1}} e^{-j(\varphi_N - \varphi_{N-1})} - \mathrm{j}\,\mathrm{cotan}(\phi_N)\overline{V_N}$$

Rearranging the previous equation we finally obtain

$$\boxed{Y_o^{-1}\overline{I_{in}} e^{j(\psi - \varphi_N)} = [gp + gL + \mathrm{j}(bp + bL - \mathrm{cotan}(\phi_N))]\overline{V_N} + \mathrm{j}[\mathrm{cosec}(\phi_N)]\overline{V_{N-1}} e^{-j(\varphi_N - \varphi_{N-1})}}$$

(3.31)

The General Case

Equations (3.20), (3.25) and (3.31) are for different ranges of k. Representing all three expression in one, we write:

$$\delta_{k,N}\, Y_o^{-1} I_{in} e^{j(\psi - \varphi_N)} = j\Theta_k \overline{V_{k-1}} e^{-j(\Delta_{k,k-1})} + [gp + \delta_{k,N} gL + j\, b_k] \overline{V_k} + j\Theta_{k+1} \overline{V_{k+1}} e^{j(\Delta_{k+1,k})}$$

where

$\delta_{k,N}$ is the Kronecker delta defined as

$$\delta_{k,N} = \begin{cases} 1 & \text{if } k = N \\ 0 & \text{if } k \neq N \end{cases},$$

$$\Theta_k = \begin{cases} \operatorname{cosec}(\phi_k) & \text{if } 2 \leq k \leq N \\ 0 & \text{if } k = 1 \end{cases}$$

$$\Delta_{m,n} = \varphi_m - \varphi_n,$$

and,

$$b_k = \begin{cases} -\operatorname{cotan}(\phi_k) - \operatorname{cotan}(\phi_{k+1}) + bp & \text{if } 1 \leq k \leq N\text{-}1 \\ -\operatorname{cotan}(\phi_N) + bp + bL & \text{if } k = N \end{cases}$$

Design for Perfect Power Dividing / Combining

To divide the input power equally without reflection, two conditions must be met. The first condition is that the sum of all the powers delivered to each probe-pair is equal to the input power. The second condition is that the amplitudes of all node

voltages must be equal. To maximize the power delivered to the probe pairs, the input admittance must be conjugate matched to that of the generator, in this case the central probe admittance. Under the conjugate matching condition, the input power may be shown to be

$$P_{in} = \frac{I_{in}^{\ 2}}{8gL\ Y_o} \qquad (3.32)$$

The average power delivered to a given probe pair with node voltage V_k is

$$P_{probe} = \frac{1}{2} gp\ Y_o\ V_k^{\ 2} \qquad (3.33)$$

In fact, this is the average power delivered to any probe pair, as we require that all node voltages be equal. That is:

$$V_1 = V_2 = ... = V_k, \quad 1 \le k \le N \qquad (3.34)$$

Equating the input power to the sum of the power delivered to each probe pair, we find

$$P_{in} = \sum_{i=1}^{N} P_{probe_i} \Rightarrow P_{in} = N\ P_{probe} \quad (3.35)$$

Conjugate matching requires that

$$gL = N\ gp$$

Replacing the above equation in (3.35) we get

$$I_{in} = 2\ NgpY_oV_k \quad (3.36)$$

We want to come up with a design such that when values of g_p and b_p are specified, those of the load admittance $gL + j\,bL$ and electrical lengths $\phi_1, \phi_2, ... \phi_N$ can be

calculated. To do that, let us first consider the case when there are four probes (i.e. N=1). Figure 3.7 shows the equivalent half circuit.

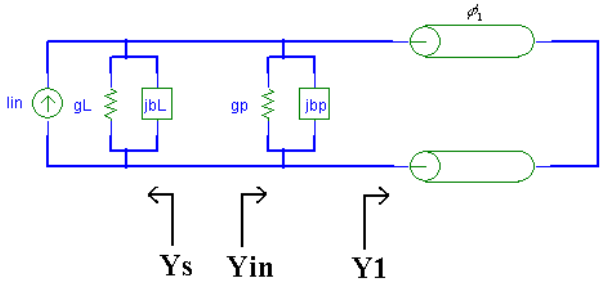

Figure 3.7 Equivalent Circuit for the case N=1.

The admittance Y_1 can be found using (3.14). Thus we can write Y_{in} and Y_s as shown below:

$$Y_1 = -j\,\mathrm{cotan}(\phi_1)$$

$$Y_{in} = gp + j[bp - \mathrm{cotan}(\phi_1)]$$

and

$$Y_S = gL + j\,bL$$

For maximum power transfer, the source admittance has to be conjugate matched to the input admittance. In this case we have

$$Y_S = Y_{in}^{*} \Rightarrow gL + j\,bL = gp + j[\mathrm{cotan}(\phi_1) - bp]$$

Accordingly we deduce that

$$\begin{cases} gL = gp \\ bL = \mathrm{cotan}(\phi_1) - bp \end{cases} \qquad (3.37)$$

Before we step forward in our design, let us go back to (3.20), (3.25) and (3.31), which represent our node equations. Since i_{in} is given by (3.36), we can substitute it in (3.31). In the derivation that follows, we make use of the fact that all node voltages are of equal amplitude. For now, let us assume that the sinusoidal voltages applied at each probe pair are in phase. Later in the chapter, the case of phase variation among the probe pairs will be examined.

For $1 \le k \le N$ we get :

$k = 1$: $gp + j[-\text{cotan}(\phi_1) - \text{cotan}(\phi_2) + \text{cosec}(\phi_2) + bp] = 0$

$k = 2$: $gp + j[-\text{cotan}(\phi_2) - \text{cotan}(\phi_3) + \text{cosec}(\phi_2) + \text{cosec}(\phi_3) + bp] = 0$

$k = 3$: $gp + j[-\text{cotan}(\phi_3) - \text{cotan}(\phi_4) + \text{cosec}(\phi_3) + \text{cosec}(\phi_4) + bp] = 0$

| |

| |

| |

$k = N - 1$: $gp + j[-\text{cotan}(\phi_{N-1}) - \text{cotan}(\phi_N) + \text{cosec}(\phi_{N-1}) + \text{cosec}(\phi_N) + bp] = 0$

$k = N$: $gp + gL + j[-\text{cotan}(\phi_N) + \text{cosec}(\phi_N) + bp + bL] = 2N\,gp$

Summing everything up from k=1 up to k=N we get

$$N\,gp + gL + j[-\text{cotan}(\phi_1) - 2\sum_{i=2}^{N}\text{cotan}(\phi_i) + 2\sum_{i=2}^{N}\text{cosec}(\phi_i) + N\,bp + bL] = 2Ngp \qquad (3.38)$$

Solving, we obtain

$$\begin{cases} N\,gp + gL = 2N\,gp & (3.39) \\ -\text{cotan}(\phi_1) - 2\sum_{i=2}^{N}\text{cotan}(\phi_i) + 2\sum_{i=2}^{N}\text{cosec}(\phi_i) + N\,bp + bL = 0 & (3.40) \end{cases}$$

Equation (3.39) verifies our previous assumption and yields our first design equation:

$$gL = N\,gp \qquad (3.41)$$

From (3.38) we can see that:

$$-\text{cotan}(\phi_1) - 2\sum_{i=2}^{N}\text{cotan}(\phi_i) + 2\sum_{i=2}^{N}\text{cosec}(\phi_i) + \text{N bp} + \text{bL} = 0 \qquad (3.42)$$

Using the fact that

$$\text{bL} = \text{cotan}(\phi_1) - \text{bp},$$

we can write that

$$2\sum_{i=2}^{N}\text{cotan}(\phi_i) - 2\sum_{i=2}^{N}\text{cosec}(\phi_i) = (\text{N} - 1)\,\text{bp} \qquad (3.43)$$

Going back to our previous sum (3.38), but this time adding everything up to some k, where $2 \le k < N$, the following is obtained:

$$(\text{k} - 1)\,\text{gp} + \text{j}[-\text{cotan}(\phi_1) - 2\sum_{i=2}^{k-1}\text{cotan}(\phi_i) + 2\sum_{i=2}^{k-1}\text{cosec}(\phi_i) - \text{cotan}(\phi_k) + \text{cosec}(\phi_k) + (k-1)\,\text{bp}] = 0$$

Completing the sum until k factors we

get

$$(\text{k} - 1)\,\text{gp} + \text{j}[-\text{cotan}(\phi_1) - 2\sum_{i=2}^{k}\text{cotan}(\phi_i) + 2\sum_{i=2}^{k}\text{cosec}(\phi_i) + (k-1)\,\text{bp} + \text{cotan}(\phi_k) - \text{cosec}(\phi_k)] = 0$$

By using (3.43) in the above equation we get:

$$(\text{k} - 1)\,\text{gp} + \text{j}[-\text{cotan}(\phi_1) + \text{cotan}(\phi_k) - \text{cosec}(\phi_k)] = 0 \qquad (3.44)$$

Writing (3.44) for different values of k, we obtain the following:

For $k' \geq 2$ we get :

$k = 2:$ $\quad 1\,gp + j[-\text{cotan}(\phi_1) + \text{cotan}(\phi_2) - \text{cosec}(\phi_2)] = 0$

$k = 3:$ $\quad 2\,gp + j[-\text{cotan}(\phi_1) + \text{cotan}(\phi_3) - \text{cosec}(\phi_3)] = 0$

$k = 4:$ $\quad 3\,gp + j[-\text{cotan}(\phi_1) + \text{cotan}(\phi_4) - \text{cosec}(\phi_4)] = 0$

| |

| |

| |

$k = k':$ $\quad (k'-1)\,gp + j[-\text{cotan}(\phi_1) + \text{cotan}(\phi_{k'}) - \text{cosec}(\phi_{k'})] = 0$

Summing everything up and once again using (4.43), we get

$$gp[1+2+\ldots+(k'-1)] + j[-(k'-1)\,\text{cotan}(\phi_1) + \frac{k'-1}{2}\,bp] = 0$$

Ensuring that the imaginary term equals to zero, we get a second design equation:

$$\text{cotan}(\phi_1) = \frac{bp}{2}. \qquad (3.45)$$

Since

$$bL = \text{cotan}(\phi_1) - bp,$$

we also obtain

$$bL = -\frac{bp}{2}. \qquad (3.46)$$

Going back to (3.44) we write

$$(k-1)\,gp + j[-\text{cotan}(\phi_1) + \text{cotan}(\phi_k) - \text{cosec}(\phi_k)] = 0$$

therefore,

$$(k-1)\,gp + j[-\frac{bp}{2} + \operatorname{cotan}(\phi_k)] = j\operatorname{cosec}(\phi_k)$$

Taking the absolute value of everything:

$$|(k-1)\,gp + j[-\frac{bp}{2} + \operatorname{cotan}(\phi_k)]|^2 = |j\operatorname{cosec}(\phi_k)|^2$$

$$(k-1)^2 gp^2 + (\frac{bp}{2})^2 - 2\frac{bp}{2}\operatorname{cotan}(\phi_k) + \operatorname{cotan}^2(\phi_k) = \operatorname{cosec}^2(\phi_k)$$

$$(k-1)^2 gp^2 + (\frac{bp}{2})^2 - bp\operatorname{cotan}(\phi_k) = -\operatorname{cotan}^2(\phi_k) + \operatorname{cosec}^2(\phi_k)$$

Because

$$-\operatorname{cotan}^2(\phi) + \operatorname{cosec}^2(\phi) = 1$$

we finally get

$$(k-1)^2 gp^2 + (\frac{bp}{2})^2 - bp\operatorname{cotan}(\phi_k) = 1$$

Accordingly for $2 \le k \le N$ we get:

$$-\operatorname{cotan}(\phi_k) = \frac{1}{bp}[1 - (\frac{bp}{2})^2 - (k-1)^2 gp^2] \qquad (3.47)$$

Incorporating previous results we can write

$$-\operatorname{cotan}(\phi_k) = \begin{cases} -\dfrac{bp}{2} & (k=1) \\ \dfrac{1}{bp}[1 - (\dfrac{bp}{2})^2 - (k-1)^2 gp^2] & (2 \le k \le N) \end{cases} \qquad (3.48)$$

Now we have a powerful tool to properly design our system. Different values of electrical lengths of multiple transmission lines can be calculated and tuned to meet the design equations of (3.48).

Out-of-Phase Waves

In the previous work we assumed that all the sinusoid voltages were inphase. Now we can investigate how phase can play a role in our design equations. First we rewrite the node equations but this time taking into account the phase.

For the case when k=1

$$\begin{aligned} &gp - j\,\mathrm{cotan}(\phi_1) + j\,bp - j\,\mathrm{cotan}(\phi_2) + j\,\mathrm{cosec}(\phi_2)e^{j(\varphi_2-\varphi_1)} = 0 \\ &gp - j[\,bp - \mathrm{cotan}(\phi_1) - \mathrm{cotan}(\phi_2) + \mathrm{cosec}(\phi_2)e^{j(\varphi_2-\varphi_1)}] = 0 \end{aligned}$$

However, we know that:

$$e^{j(\varphi_x-\varphi_y)} = \cos(\varphi_x-\varphi_y) + j\sin(\varphi_x-\varphi_y)\,;$$

Thus

$$gp - j[\,bp - \mathrm{cotan}(\phi_1) - \mathrm{cotan}(\phi_2) + \cos(\varphi_x-\varphi_y)\,\mathrm{cosec}(\phi_2) + j\sin(\varphi_x-\varphi_y)\,\mathrm{cosec}(\phi_2)] = 0$$

Setting the real part to zero we get:

$$gp + \sin(\varphi_2-\varphi_1)\,\mathrm{cosec}(\phi_2) = 0 \qquad (3.49)$$

Doing the same thing for the remaining cases:

For $2 \le k \le N-1$:

$$j\,\mathrm{cosec}(\phi_k)e^{-j(\varphi_k-\varphi_{k-1})} + [gp - j\,\mathrm{cotan}(\phi_k) + j\,bp - j\,\mathrm{cotan}(\phi_{k+1}) + j\,\mathrm{cosec}(\phi_{k+1})\,e^{j(\varphi_{k+1}-\varphi_k)}] = 0$$

$$j\,\mathrm{cosec}(\phi_k)\cos(\varphi_k-\varphi_{k-1}) + j\,\mathrm{cosec}(\phi_k)\,j\sin(\varphi_{k-1}-\varphi_k) + gp - j\,\mathrm{cotan}(\phi_k) + j\,bp$$

$$- j\,\mathrm{cotan}(\phi_{k+1}) + j\,\mathrm{cosec}(\phi_{k+1})\cos(\varphi_{k+1} - \varphi_k) + j\,\mathrm{cosec}(\phi_{k+1})\; j\sin(\varphi_{k+1} - \varphi_k) = 0$$

Again setting the real part to zero we get

$$-\mathrm{cosec}(\phi_k)\sin(\varphi_{k-1} - \varphi_k) + gp - \mathrm{cosec}(\varphi_{k+1})\sin(\varphi_{k+1} - \varphi_k) = 0$$

Using a similar technique as before, but in this case summing the real part of each equation to get rid of some unknowns, we obtain:

$k' = 1$: $\quad gp - \sin(\varphi_2 - \varphi_1)\,\mathrm{cosec}(\phi_2) = 0$

$k' = 2$: $\quad -\mathrm{cosec}(\phi_2)\sin(\varphi_1 - \varphi_2) + gp - \mathrm{cosec}(\varphi_3)\sin(\varphi_3 - \varphi_2) = 0$

$|$ $\quad$ $|$

$|$ $\quad$ $|$

$|$ $\quad$ $|$

$k' = k - 1$: $\quad -\mathrm{cosec}(\phi_{k-1})\sin(\varphi_{k-2} - \varphi_{k-1}) + gp - \mathrm{cosec}(\varphi_k)\sin(\varphi_k - \varphi_{k-1}) = 0$

The sum yields to

$$(k-1)\,gp - \mathrm{cosec}(\phi_k)\sin(\varphi_k - \varphi_{k-1}) = 0$$

$$(k-1)\,gp = \mathrm{cosec}(\phi_k)\sin(\varphi_k - \varphi_{k-1})$$

Finally we obtain

$$\sin(\varphi_k - \varphi_{k-1}) = (k-1)\,gp\sin(\phi_k)$$

The exact technique would be used for the case of a combiner to obtain:

$$\sin(\psi_k - \psi_{k-1}) = -(k-1)\,gp\sin(\phi_k)$$

Power Distribution

In this section power flow distribution is derived. We will refer to Pf_k as the forward power traveling toward the shorting plate, and Pb_k as the backward power reflected and propagating toward the central probe in a transmission line section of electrical length ϕ_k. Figure 3.8 illustrates the situation. A good thing to notice, which could be used to verify our theory at the end, is that Pb_1 is the total reflection of Pf_1 since the shorting plate will transmit none of the incident power Pf_1.

Thus $Pf_1 = Pb_1$.

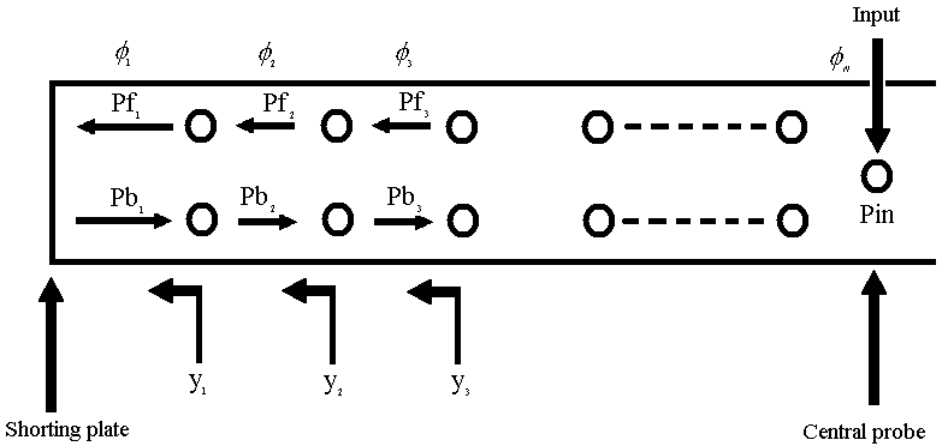

Figure 3.8 Forward and backward powers flow in half the waveguide.

The admittances [3] y_1, y_2, and y_3 can be written using (3.14), as follows:

$$y_1 = -j\cot an(\phi_1) = -j\frac{b_p}{2}$$

$$y_2 = y_1 + gp + j\,bp = gp + j\frac{b_p}{2}$$

[3] Without including the probe admittance of the same stage

$$y_3 = y_2^{*} + gp + j\,bp = gp + j\frac{b_p}{2} + gp - j\,b_p$$

$$= 2gp - j\frac{bp}{2}$$

From before it is obvious that

$$y_k = (k-1)\,gp + (-1)^k\, j\frac{bp}{2} \tag{3.46}$$

The physical meaning of y_k represents the normalized load admittance seen at some probe location with electrical length ϕ_k; therefore, the reflection coefficient will change as a function of location and we can write

$$\Gamma_k = \frac{1-y_k}{1+y_k} \Rightarrow |\Gamma_k|^2 = \frac{|1-y_k|^2}{|1+y_k|^2}$$

Substituting (3.46) in the equation above, we get

$$|\Gamma_k|^2 = \frac{|1-(k-1)\,gp + (-1)^k\, j\frac{bp}{2}|^2}{|1+(k-1)\,gp + (-1)^k\, j\frac{bp}{2}|^2}$$

$$|\Gamma_k|^2 = \frac{[1-(k-1)\,gp]^2 + (\frac{bp}{2})^2}{[1+(k-1)\,gp]^2 + (\frac{bp}{2})^2}$$

On the other hand, we have

$$\frac{Pb_k}{Pf_k} = |\Gamma_k|^2$$

Thus we obtain

$$\begin{cases} Pf_k = \frac{1}{8} Y_o V^2 [1+(k-1)\,gp]^2 + (\frac{bp}{2})^2 \\ Pb_k = \frac{1}{8} Y_o V^2 [1-(k-1)\,gp]^2 + (\frac{bp}{2})^2 \end{cases} \tag{3.47}$$

In equation (3.47) we can see that the assumption $Pf_1 = Pb_1$ is well verified.

The power flow is written as

$$\begin{aligned} P_{flow} &= Pf_k - Pb_k \\ &= \frac{1}{2}(k-1)\, gp\, Y_o V^2 \\ &= (k-1)\frac{P_{in}}{2N} \end{aligned}$$

where we had

$$P_{in} = \frac{1}{8} Y_o V^2$$

In the equation above we see that that the divider equally splits an input power into 2N portions. The perfect power division is achieved. Figure 3.7 shows the normalized power flows, the forward power and the backward power. The forward power increases with the index k. This means that the forward power is higher in magnitude near the central probe, which makes perfect sense since at that place the power does not see much reflection (assuming that there was no reflection due to impedance mismatch). The backward power however undergoes a totally opposite process; it gets higher as it propagates toward the shorting plate, i.e. k=1. On the other hand, the power flow inside the waveguide increases as it approaches the central probe due to the successive power providing to probe-pairs.

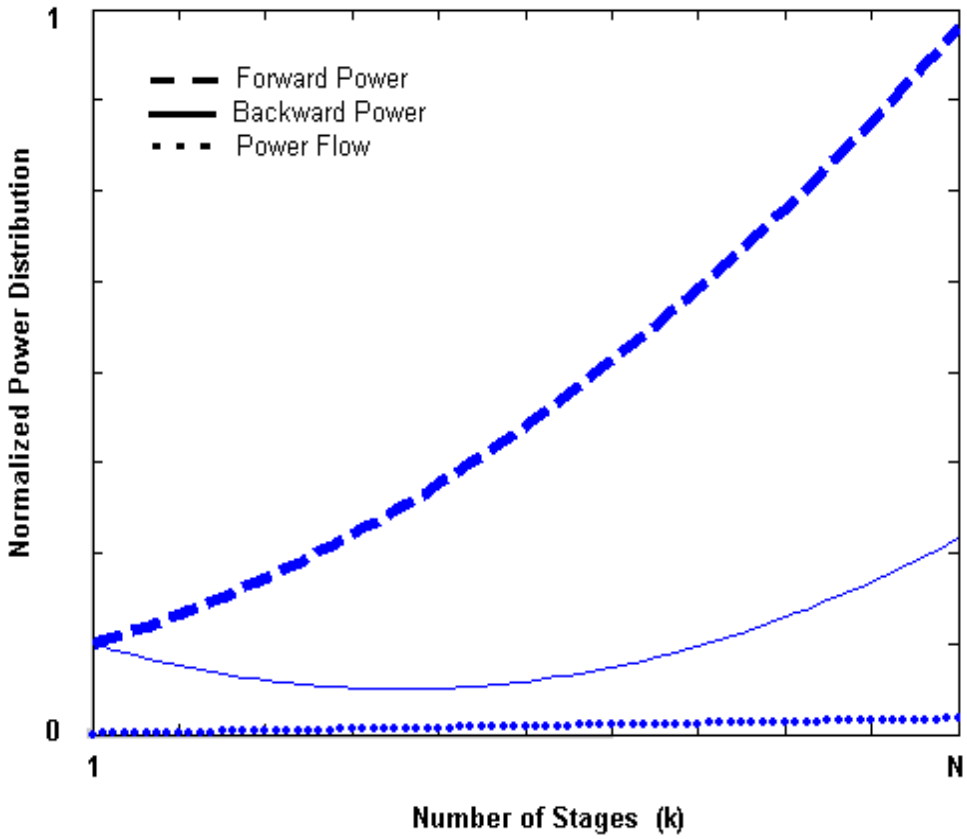

Figure 3.9 Waveguide power versus position

CHAPTER FOUR

A COAXIAL DOUBLE LADDER COMBINER

Introduction

The equivalent circuit analysis detailed in chapter 3 for the double ladder structure provides design formulas for perfect power dividing/combining operations. Figure 4.1(a) shows the coaxial double-ladder power combiner/divider of Sanada et al [6] for the case of N=1. The waveguide has been hidden in Figure 4.1 (b) to illustrate the general shape of the coaxial probes. The structure consists of two-paired coaxial cables plus an input/output probe placed at the center of the waveguide; therefore, the structure has 5 coaxial cables in total (i.e. 4N+1). The design formulas obtained in the previous chapter will provide the means for designing the waveguide dimensions and the coaxial cable positions for optimal performance. In this chapter, HFSS will be used to simulate the coaxial double ladder of Sanada et al. for the case of N=1. By doing so, this chapter will not only corroborate results found in the literature, but also begin to develop an efficient means to design double ladder power combiners. As mentioned in chapter 2, the analysis will be carried out assuming that only the dominant mode will propagate.

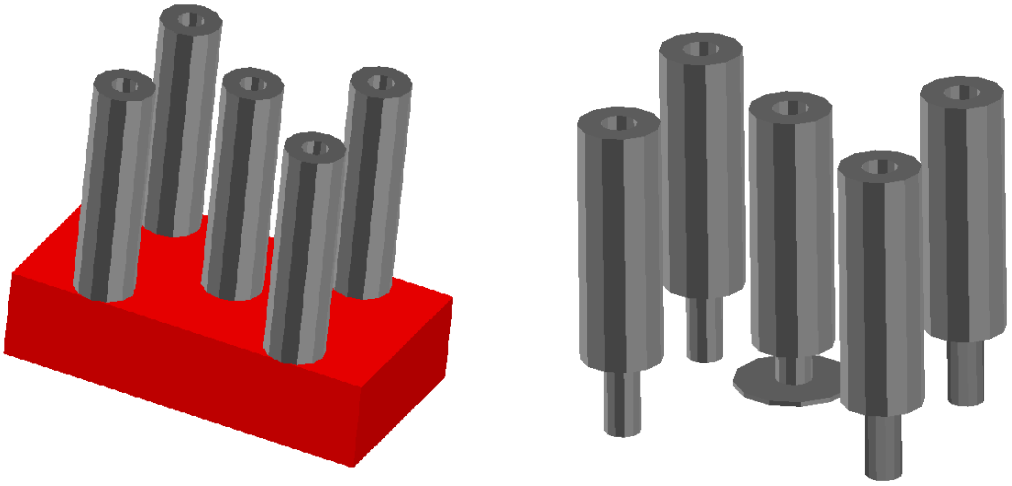

(a) Full view (b) Waveguide is hidden

Figure 4.1 The combiner/divider for the case of N=1.

The results presented in this chapter will be at X-band[4], so that comparisons may be drawn from measured results found in the literature. The design of such power combiners / dividers involves choosing the proper locations and dimensions of the cables and probes. The normalized admittance of the paired probes is a complex value that can be represented as we discussed in chapter 3, as y_p, where

$$yp = g_p + j\, b_p$$

The values of g_p and b_p, namely the probe conductance and the susceptance, are essential to our design. Once their values are selected, the geometry of the structure may be designed. A top view of a N=1 coaxial double ladder structure is illustrated in Figure 4.2. The distance between the backshort and the center of the outermost probe pair (ϕ_1), the distance of the pair from the waveguide sidewalls (s) and the geometry of the probes

[4] X-band: The frequency range between 8.20GHz and 12.4GHz.

themselves (see Figure 4.1(b)) each play a role in the value of yp. Thus we have at least these parameters to manipulate so as to realize a desired yp.

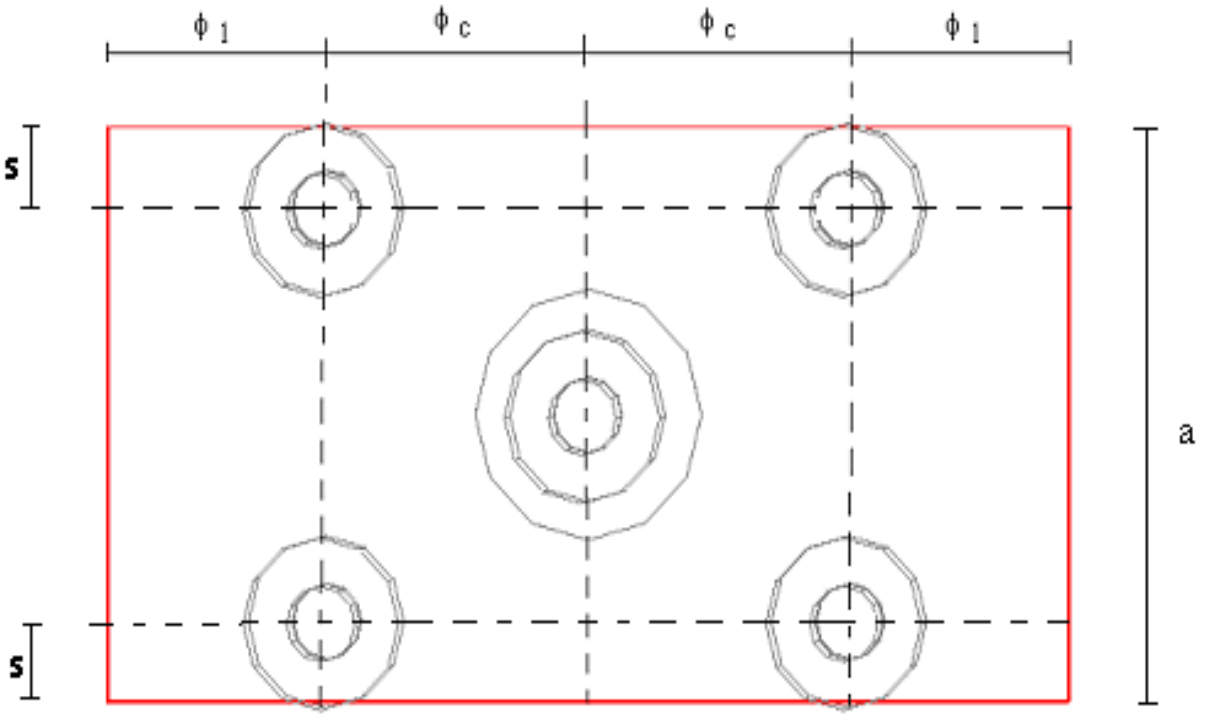

Figure 4.2 Dimensions of the waveguide (top view).

Simulation of the N=1 Coaxial Double Ladder Combiner / Divider

Given in Table 4.1 are the probe-pair and central probe characteristics as taken from table 2 of [6]. These values correspond to those used in the experiments of Sanada et al. for an N=1 structure designed for a center frequency of 9 GHz. Figure 4.3 illustrates the parameters D_1, D_2, D_{in}, D_{disk}, T and D_{out}. It is interesting to note that the central probe is of the ”doorknob” type. The doorknob probe is used for its superior power-handling capability and bandwidth [13].

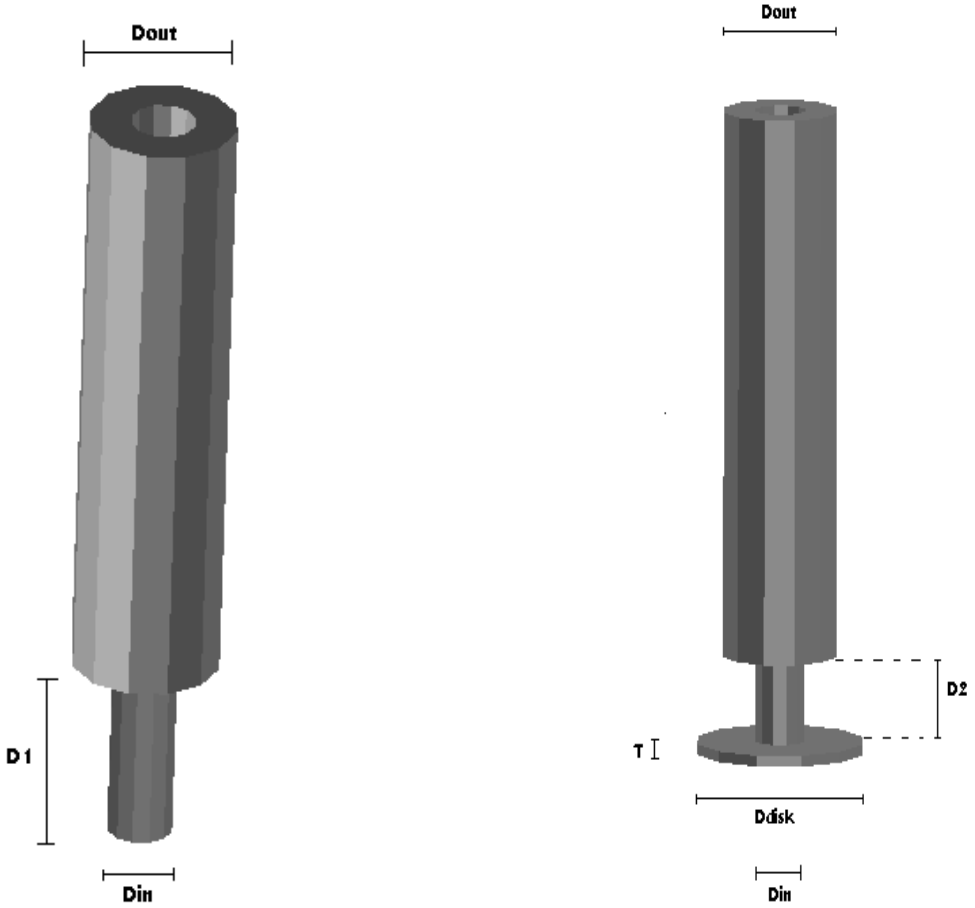

(a) Paired coaxial cable (b) Central coaxial cable

Figure 4.3 Dimensions of the probe cable.

Conspicuously missing from table 2 of [6], and thus from Table 4.1, are values of the probe diameter D_{in} and that of the coax D_{out}. In a figure in [6], it is mentioned that the connectors are SMA, and in a separate work by Fukui et al. [14] it is mentioned that 50 Ω cables are used and that D_{in}= 3 mm. Since the work of Fukui et al. is similar to that of Sanada et al., from this point on we assume Din=3 mm.

Probe-Pair				Central-Probe			
s[mm]	D_1[mm]	gp	bp	D_2[mm]	T[mm]	D_{disk}[mm]	ϕ_c[rad]
3.2	8.0	1.25	0.68	4	0.5	10	1.49

Table 4.1: Parameter values of the structure.

Using equation 3.48, we compute the electrical length ϕ_1 using data given in Table 4.1. Recall that an electrical length ϕ is related to the physical length L by:

$$\phi = \beta(\mathrm{f})\, \mathrm{L}$$

where $\beta(\mathrm{f})$ is the phase constant varying with frequency. Power is propagating in a rectangular waveguide, thus the phase constant mentioned will be:

$$\beta(\mathrm{f}) = \left| \left[\left(\frac{\pi}{\mathrm{a}} \right)^2 - k_o(\mathrm{f})^2 \right]^{0.5} \right|$$

where

a is the width of the waveguide (900 mils for X-band operation), and

$k_o(\mathrm{f}) = \frac{2\pi \mathrm{f}}{\mathrm{c}}$, c being the speed of light in vacuum (i.e. $\mathrm{c} = 3.10^8$ m/s)

From (3.48) we write

$$-\mathrm{cotan}(\phi_k) = \begin{cases} -\frac{\mathrm{bp}}{2} & (\mathrm{k} = 1) \\ \frac{1}{\mathrm{bp}}\left[1 - \left(\frac{\mathrm{bp}}{2}\right)^2 - (\mathrm{k}-1)^2 \mathrm{gp}^2\right] & (2 \le \mathrm{k} \le \mathrm{N}) \end{cases}$$

Thus,

$$\phi_1 = 1.24 \text{ rad}$$

and

$$L_1 = \frac{\phi_1}{\beta(9\text{ GHz})} = 379.3 \text{ mils}$$

A good checkpoint at this time of the analysis is to verify using the dimensions designed that we are obtaining the values of g_p and b_p we desire. For this reason we need to find the input admittance seen at the outer probe pair, as shown in Figure 4.5.

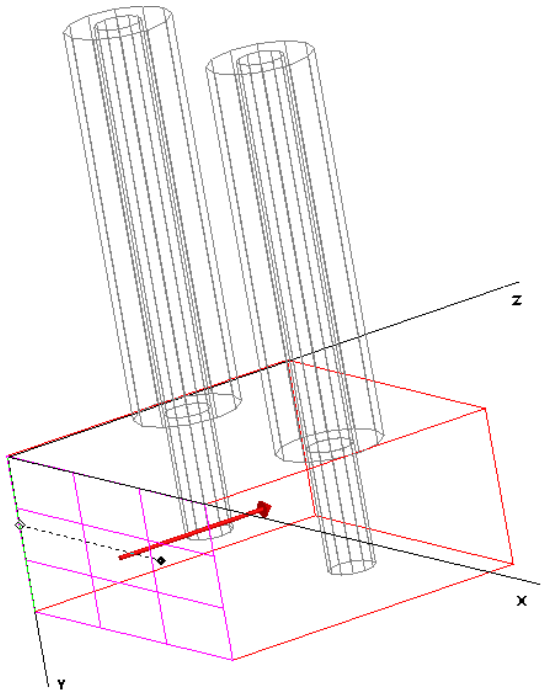

Figure 4.5 Finding the input admittance at the probe location.

The end of the arrow shown in Figure 4.5 corresponds to the location at which the admittance is determined. Throughout this thesis, admittance values are taken at the center of a given probe or probe pair. Deembedding in HFSS we obtained the S-parameters of the system at the center of the probe pair. It is relevant to note that

deembedding does not change the magnitude of the S-parameters; rather, it changes the phase only. We have proven that for N=1 the input admittance seen at the probe-pair location (including the admittance of the probe pair) toward the shorting plate is

$$b_p = \cot(\phi_1) \quad y_p = g_p + j\,[b_p - \cot(\phi_1)].$$

The admittance at a given location in the waveguide may be readily determined using the reflection scattering parameter (S_{11}) at the location using the simple equation

$$y_p = \frac{1 - S_{11}}{1 + S_{11}}$$

Taking into account that

$$b_p = 2\cot(\phi_1),$$

we can verify that the calculated g_p and b_p calculated are close to the designed values. To do so, the deembedded S-parameters were then imported to MATLAB, converted to normalized admittance values and plotted in Figure 4.6.

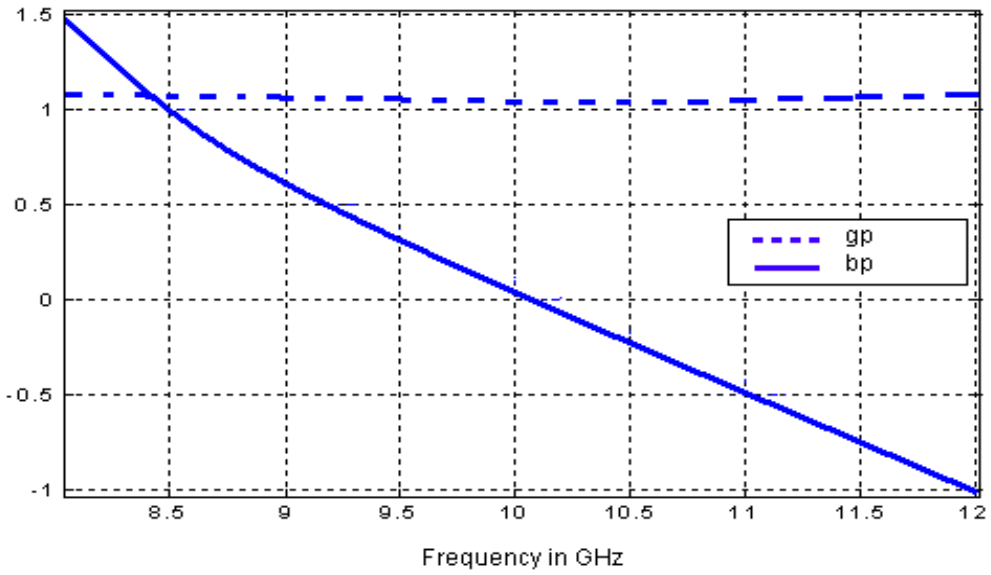

Figure 4.6 gp, bp and 2cotan(ϕ_1) as a function of frequency.

Figure 4.6 shows very important results, in that the values of g_p and b_p obtained around 9 GHz are very close to the values with which we started. This fact provides some evidence that our deembedding technique is effective. A second point to be made from the results of figure 4.6 is that the probe admittance is frequency dependent.

Sizing the Cables

For a coaxial cable shown in Figure 4.7, the characteristic impedance is given by

$$Z_o = \frac{138}{\sqrt{\varepsilon_r}} \log_{10}\left(\frac{D}{d}\right), \qquad (4.1)$$

where D is the inner diameter of the outer conductor, d is the outer diameter of the inner

conductor and ε_r is the relative dielectric constant of the material separating the center and outer conductors.

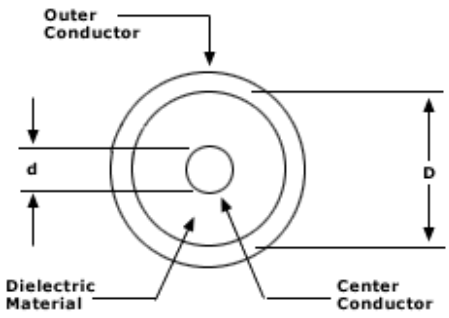

Figure 4.7 Top view of a coax cable.

Impedance matching requires the cables to be 50 ohms to keep reflection losses to a minimum. For this reason the inner and the outer diameter are 117 mils and 270 mils, respectively. Assuming that the material used as the dielectric is air (i.e. $\varepsilon_r=1$), equation (4.1) gives the

following cable characteristic impedance:

$$Z_o = 50.11\ \Omega .$$

To insure that our assumption of single-mode propagation is upheld, we must use caution in choosing the inner and the outer diameter of the cable. Accordingly since the cutoff frequency[5] of higher-order modes is directly related to the size of the cable, we can adjust the cable dimensions so that higher-order modes occur outside our frequency range (X-band). Since we want the cables to operate with only the dominant TEM mode, we must operate the cables at frequencies below cutoff of the second mode.

In a coaxial cable this cutoff frequency is given by:

[5] The cutoff is the frequency above which other than the TE10 mode may occur

$$f_{cutoff} = \frac{2\,c}{\pi\sqrt{\varepsilon}}\frac{1}{D+d}, \qquad (4.2)$$

where ε is the dielectric constant of the material and c is the speed of light. Substituting our values to (4.2) yields a cutoff frequency of

$$f_{cutoff} = 19.43\,\text{GHz}.$$

This value is well above 12 GHz, which is the upper limit of our frequency range, So the cables not only assure the impedance wanted, but also suppress undesired modes. Table 4.2 displays a summary of the cable dimensions.

Inner diameter [mils]	Outer diameter [mils]	Cable length [mils]
117	270	1000

Table 4.2: Summary of the cable dimensions.

Note that the cable length was set to 1000 mils. The length of the coax affects neither the impedance of the cables nor the cutoff frequency; rather, it only affects the phase at which the electromagnetic waves arrive inside the waveguide, which could be verified using equations (4.1) and (4.2). Gathering the data from table 4.1 and 4.2, the structure was drawn in HFSS and simulated.

Simulation Results

In the case of N=1 we have a 4-way power splitter, therefore we expect the insertion loss to be

$$10\log(\frac{1}{4}) = -6 \text{ dB}$$

In addition, the lowest value of S_{11} should be around the desired frequency of 9 GHz, verifying a minimum reflection loss. Figure 4.8 shows the full wave simulation results for the system; specifically, the HFSS-derived scattering parameters are given. In the figure, S_{11} corresponds to the reflection at the center port, and S_{21} represents the insertion loss between ports one (i.e. the center port) and port 2. The remaining scattering parameters are defined in a similar fashion.

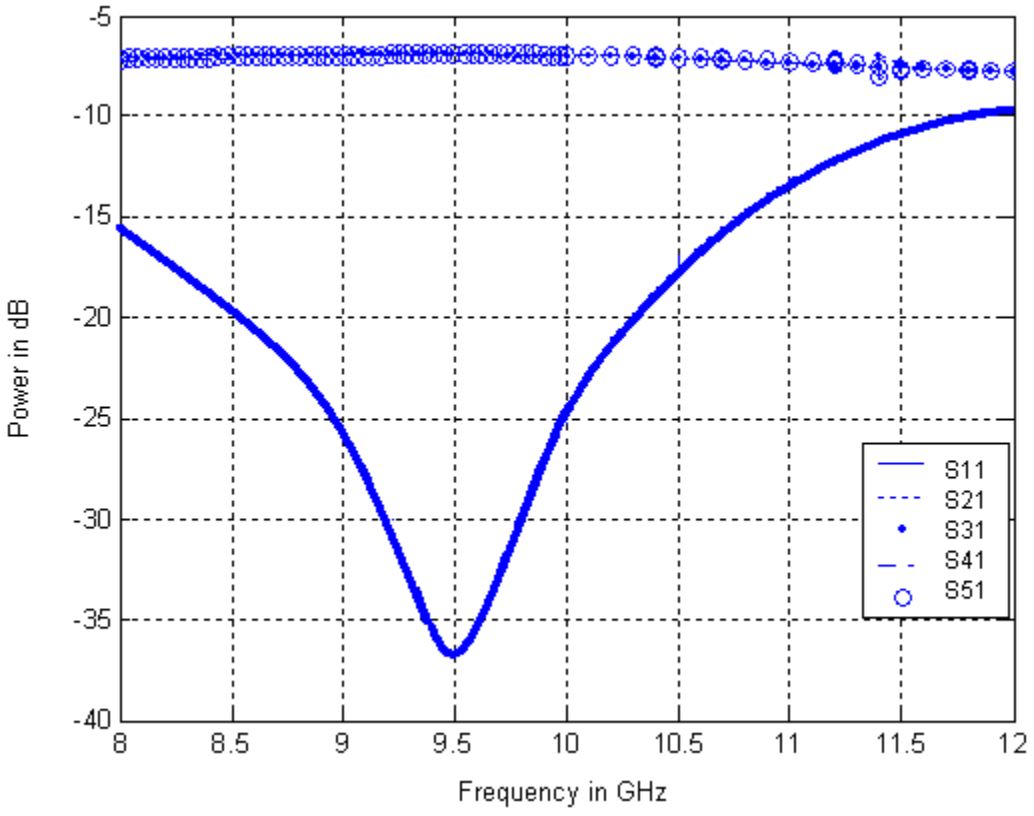

Figure 4.8 S Parameters of the four-way combiner divider.

Among the important characteristics of efficient power divider / combiner system are equal power division and broad bandwidth. Figure 4.8 demonstrates that the 4-way combiner / divider exhibits relatively broad bandwidth. For example, its 15 dB return loss bandwidth is approximately 30% and its 0.5 dB insertion loss bandwidth (relative to the generic –6 dB level of a 4-way structure) is approximately 50%. Figure 4.9 represents a smith chart used to locate the reflection coefficient, S_{11}.

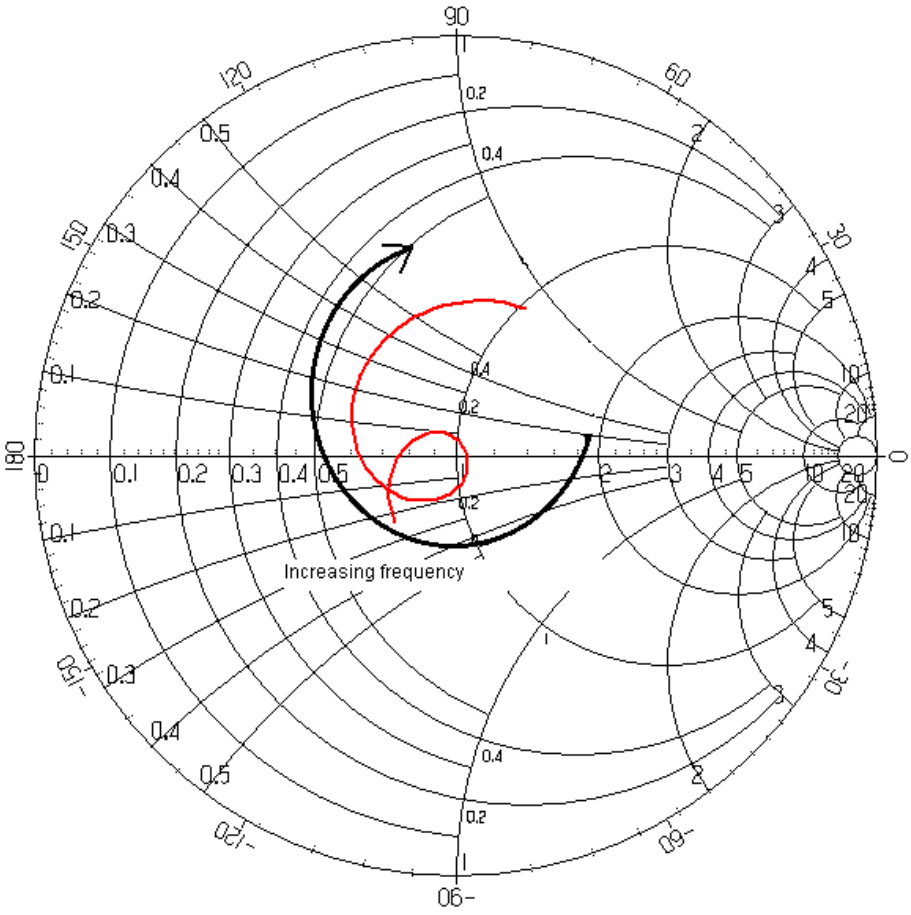

Figure 4.9 Plot of S11 on a Smith Chart.

The trace approaches the center, which is the place for perfect matching, at approximately 9.5 GHz. That the minimum return loss occurs at 9.5 GHz instead of the anticipated 9GHz is likely because our structure's geometry is not precisely that used by Sanada et al. (some geometric details were left out in the paper) and because movable backshorts were used by Sanada to tune the structure.

In this chapter, simulation of an N=1 combiner / divider was detailed. In the next chapter, the approach developed in chapter 3 will be put to a test so as to produce a combiner / divider that performs in the same fashion as the one just presented, but that is designed in a manner such that it could be implemented for use at frequencies above 100 GHz using a micromachining process such as those described in [4] and [5].

CHAPTER FIVE

A PLANAR PROBE DOUBLE LADDER WAVEGUIDE POWER DIVIDER

Introduction:

A broadband waveguide-based microwave divider/combiner structure, named the double ladder, was demonstrated numerically in the previous chapter. That structure consisted of a rectangular waveguide cavity fed by a coaxial probe at the center, surrounded on both sides by coaxial probe pairs to achieve four-way power splitting (N=1).

In this chapter we design a power combining / dividing structure analogous to the coaxial double ladder using a similar technique and design methodology as developed in both chapters 3 and 4. The structure we are proposing operates by injecting microwave power inside the cavity of a WR-430[6] waveguide through the use of planar transmission lines and probes. The goal is make the frequency of operation around 2.24 GHz and achieve perfect power splitting with the widest bandwidth possible. An illustration of the proposed structure is shown in Figure 5.1.

[6] WR-430: Rectangular waveguide to be operated at 1.70-2.60 GHz

Designing the System

The approach chosen was developed in chapter 3 and used in chapter 4 for the coaxial double ladder.

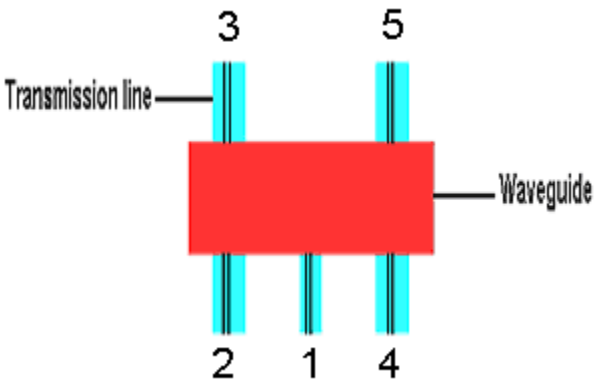

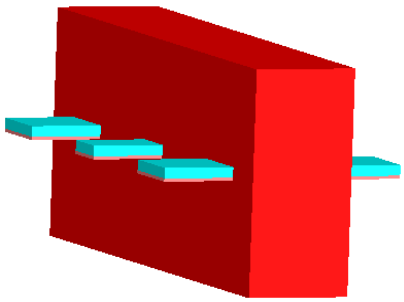

Figure 5.1 (a): Top view. Figure 5.1 (b): Side view (3D).

Figure 5.1 Different views of the coplanar combiner/divider.

The technique consists of obtaining an equivalent circuit of the system, from which the admittances of the planar transmission lines and probes determine design values for separation distances that are shown in Figure 5.2. The transmission lines penetrate the waveguide and their probes act like radiating antennas. The location and dimensions of the probes determine the value of g_p and b_p and accordingly, also affect the bandwidth of the combiner / divider.

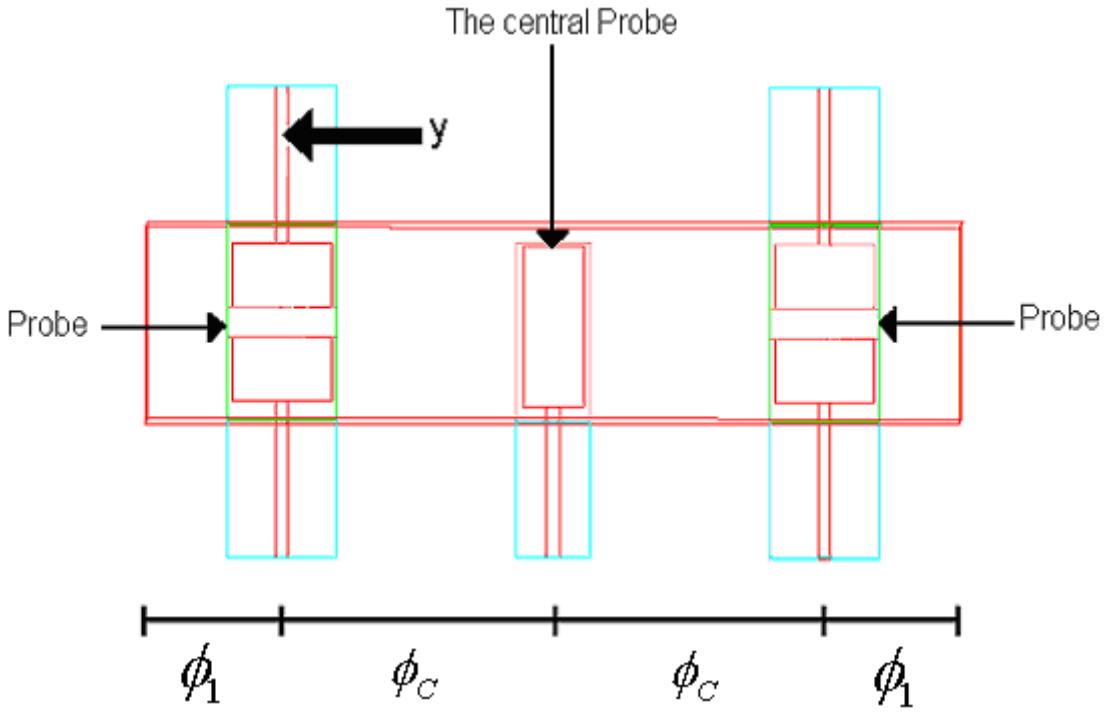

Figure 5.2 Top view of the 4-way planar power combiners / divider.

As illustrated in Figure 5.2, the electrical length between the waveguide back-short and the outer probe pair, ϕ_1, is taken as the distance from the rear side of the waveguide up to the center of the probe pair. On the other hand the distance from the center of the probe pair to the center of the input probe is denoted ϕ_C. For convenience and clarity, the same terminology used for the coaxial double ladder combiner is used for the planar structure.

Once probe admittances were selected, electrical lengths could be obtained using (3.48), which is stated below for convenience.

$$-\operatorname{cotan}(\phi_k) = \begin{cases} -\dfrac{bp}{2} & (k = 1) \\ \dfrac{1}{bp}\left[1 - \left(\dfrac{bp}{2}\right)^2 - (k-1)^2 gp^2\right] & (2 \le k \le N) \end{cases}$$

Finally *High Frequency Structure Simulator* (HFSS) was used to run a full-wave simulation of the combiner/divider to verify the performance and frequency response. *Advanced Design System* (ADS) [15] was used to simulate the equivalent circuit proposed for the system. Results obtained from of the latter simulator were compared against the former.

In Figure 5.2, the normalized admittance[7] y seen left from the center of the left-hand probe pair is given by

$$y = g_p + \mathrm{j}b_\mathrm{p} - \mathrm{j}\ \mathrm{cotan}(\phi_1), \qquad (5.1)$$

where g_p and b_p are the normalized conductance and susceptance of the probe respectively. Note that this equation was derived earlier in chapter 3. The admittance seen at the center of waveguide, is given by

$$y_{center} = \frac{y - \mathrm{j}\tan(\phi_c)}{1 - \mathrm{j}\, y \tan(\phi_c)}. \qquad (5.2)$$

As the central probe sees probe pairs in a parallel combination (one to the left in Figure 5.2 and one to the right), with each probe having the same admittance, for matching we require the central probe admittance, y_{cp}, to be given by

$$y_{cp} = 2y_{center}\ *$$

Since

$$\tan(\phi_c) = 0,$$

[7]normalized admittance: every admittance, susceptance or conductance is normalized to the waveguide admittance.

The central probe admittance is

$$y_{cp} = y;$$

finally,

$$y_{cp} = 2[g_p - jb_p + j \cot(\phi_l)]. \qquad (5.3)$$

With the appropriate design equations in hand, we are able to begin the design. Typically, the design process begins by choosing values for the normalized probe admittance. In the case to be described, assuming that it is possible to accurately realize any given probe admittance via HFSS, we choose a desired probe admittance y_p to achieve a desired bandwidth for a given order N. The following design steps were taken to realize the desired probe admittance:

1. To achieve desired bandwidth for a given order N, choose

$$y_p = g_p + j\, b_p$$

2. Calculate the ϕ_k's for k = 1, 2, ….N using (3.48).

3. Calculate necessary "load admittance" given by

$$y_l = N g_p - j \frac{b_p}{2}$$

4. Decide on ϕ_c. In general, smaller ϕ_c gives better bandwidth. Naturally, ϕ_c is limited by probe size and perhaps obfuscating coupling effects.

5. Calculate necessary central probe admittance based on y_{center}:

$$y_{cp} = g_{cp} + j\, b_{cp} = 2\left[\frac{y - j \tan(\phi_c)}{1 - j\, y \tan(\phi_c)}\right]$$

6. Realize probe admittances using full wave simulation.

7.

The design to be presented uses the equations that are given above but strays somewhat from the outlined steps. This was necessary because previously machined waveguide blocks were to be used, thus constraining the choice of L_1 and L_c. The blocks had L_c=3330 mils and L_1=1670 mils. As discussed earlier, a convenient choice for ϕ_C is 180°. Based on the machined waveguide, L_c= 3330 mils corresponds to ϕ_C =180° at 2.24 GHz. The following demonstrates this fact.

The physical length may be obtained from

$$\phi_c = \beta(\mathrm{f})\, \mathrm{L_c}.$$

Recall that $\beta(\mathrm{f})$ is the phase constant in rectangular waveguide and is given by

$$\beta(\mathrm{f})=|[(\frac{\pi}{\mathrm{a}})^2 - k_o(\mathrm{f})^2]^{0.5}|,$$

where

a is the width of the WR-430 waveguide (4300 mils for R-band operation), and

$k_o(\mathrm{f})=\frac{2\pi \mathrm{f}}{\mathrm{c}}$, c being the speed of light in vacuum (i.e. c=$3.10^8 m/s$).

Using the above equations, for a design frequency of 2.24 GHz, we obtained

$$\mathrm{L_c} = 3330 \text{ mils}.$$

The distance separating the backshort and the center of the probe pair, ϕ_1, was found to correspond to 90^o at 2.24 GHz.

Using the same method as before, we obtain

$$\mathrm{L_1} = 1670 \text{ mils}.$$

The next step in the design was to choose the probe pair susceptance and conductance. The probe pair susceptance, b_p, was taken to be zero according to design equation (3.48) and the value of g_p was varied. This method was used to determine the range of g_p required to realize a broad matching bandwidth. A contour plot was later obtained to show the behavior of the bandwidth as the probe pair admittance changed.

The structure resulting from the procedure outlined above was drawn and simulated in HFSS. Figure 5.3 shows the geometry that was used to design the central probe and the other two probe-pairs.

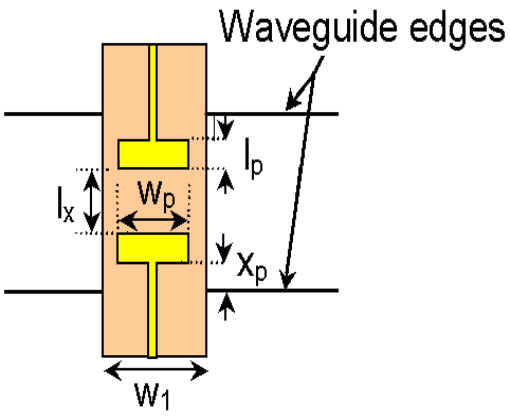

Figure 5.3 (a): Outer probe-pair.

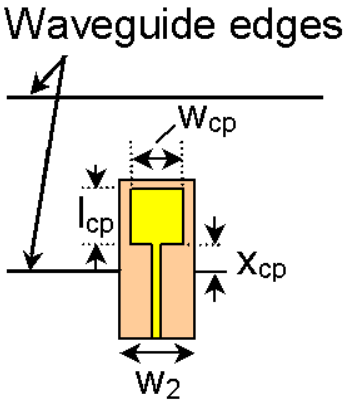

Figure 5.3 (b): Central probe.

Figure 5.3 Probe designs.

The dimensions shown above determine the admittance of both the central and the outer probes, thus they play a significant role in obtaining a broadband performance. The dimensions of the microstrip feed were designed to obtain a 50 Ω impedance. The metal traces were realized on a 0.060 inch thick duroid substrate with a relative permittivity of

2.94. A trace width of 151 mils on such a substrate results in a 50 Ω characteristic impedance. Table 5.1 and 5.2 summarizes the dimensions used in this design.

l_p	W_p	X_p	W_1	l_x
700	1200	210	1350	2480

Table 5.1: Dimensions of the outer probe-pair, in mils.

l_{cp}	W_{cp}	X_{cp}	W_2
1750	750	150	900

Table 5.2: Dimensions of the central probe, in mils.

Full Wave Simulation

Figure 5.4 shows the S parameters of the combiner/divider obtained from HFSS. S_{11} refers to the reflection at the center port in using the structure as a divider, S_{21} refers to the insertion loss between ports 1 and 2, S_{31}, S_{41} and S_{51} are insertion losses between port 1 and port 3, port 4 and port 5, respectively.

In the case of N=1, we have a four-to-one power splitter; therefore we expect the insertion loss to be

$$10\log(\frac{1}{4}) = -6 \text{ dB}$$

According to the design procedure, we must expect the best match to happen around 2.24 GHz. This is clearly observed in Figure 5.4, where we can see that S_{11} drops to its lowest

value around that frequency (recall that S_{11} is the reflection coefficient seen at the central probe).

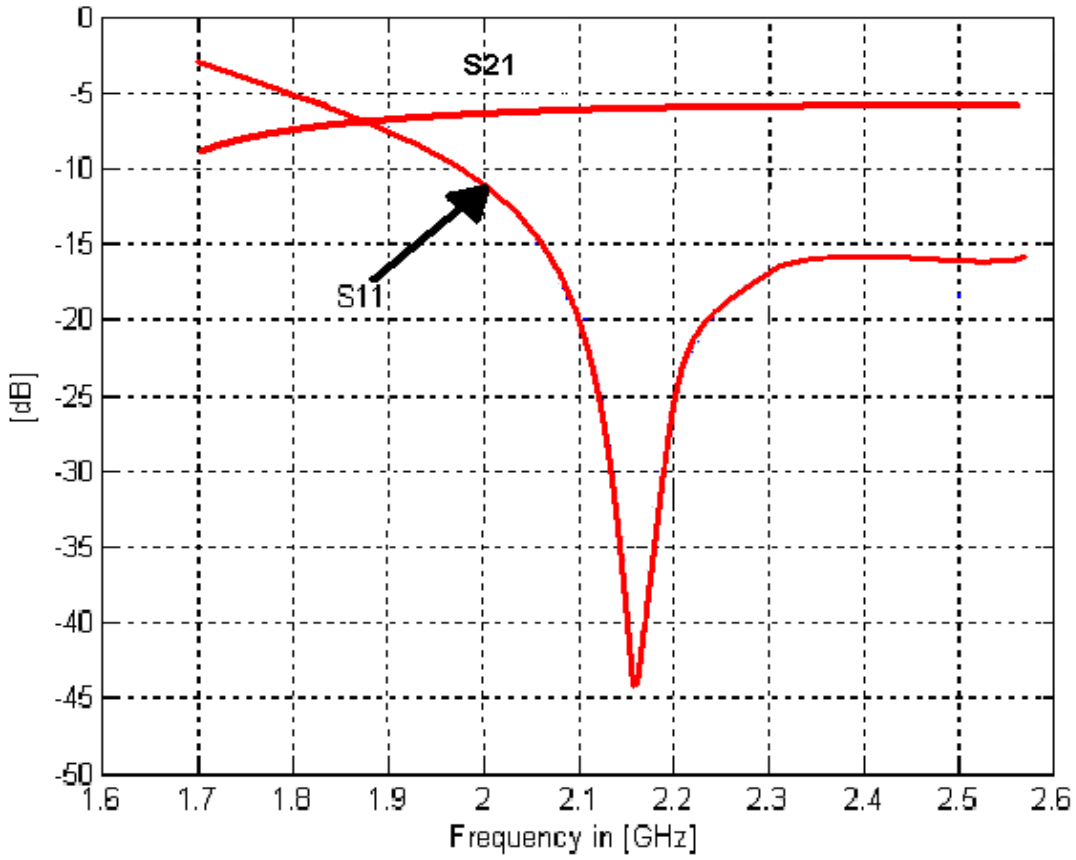

Figure 5.4 Simulated results in dB.

Another important aspect of the design is present in Figure 5.4: the values of S_{21}, S_{31}, S_{41} and S_{51} are roughly equal, which means that power is being split almost equally four ways. However, it is important to observe that power division is not perfectly equal; rather, the power delivered to ports 3 and 5 (see Figure 5.1 for port numbers) from the

central probe is greater than that delivered to the other two ports. The difference was observed to be around 0.25 dB, as shown in Figure 5.5. This imperfection is caused by the lack of complete symmetry in the microstrip version, whereas the double ladder coaxial version was perfectly symmetrical along the length and width of the waveguide.

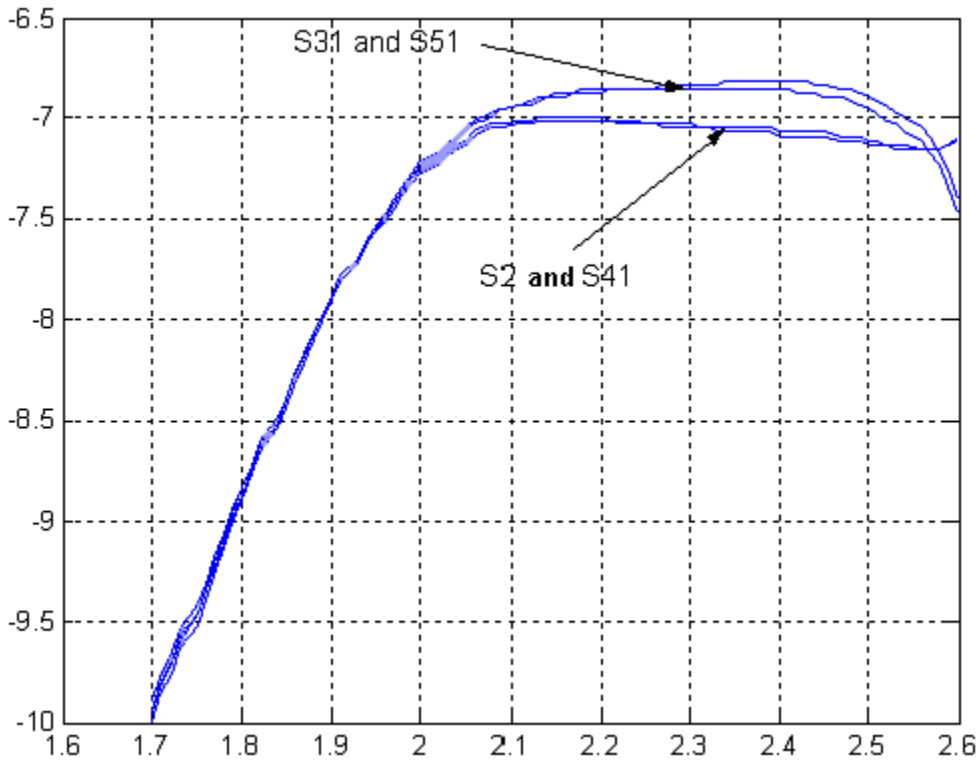

Figure 5.5 Insertion loss results for the 4-way combiner / divider.

Because the microstrip version loses symmetry along the length of the waveguide, we have observed that S_{21} roughly equals S_{41} and S_{31} equals S_{51} but S_{21} and S_{31} are not quiet equal. The problem could be solved by using either an asymmetric probe

design in order to compensate for the power difference, or by placing an iris so as to control the magnetic flux propagation inside the cavity.

The results obtained from the full-wave simulation could also permit us to verify our earlier assumptions about the probe pair admittance; thereby, obtaining actual values for g_p and b_p. For this reason, the input admittance seen at the location shown Figure 5.6 needs to be calculated.

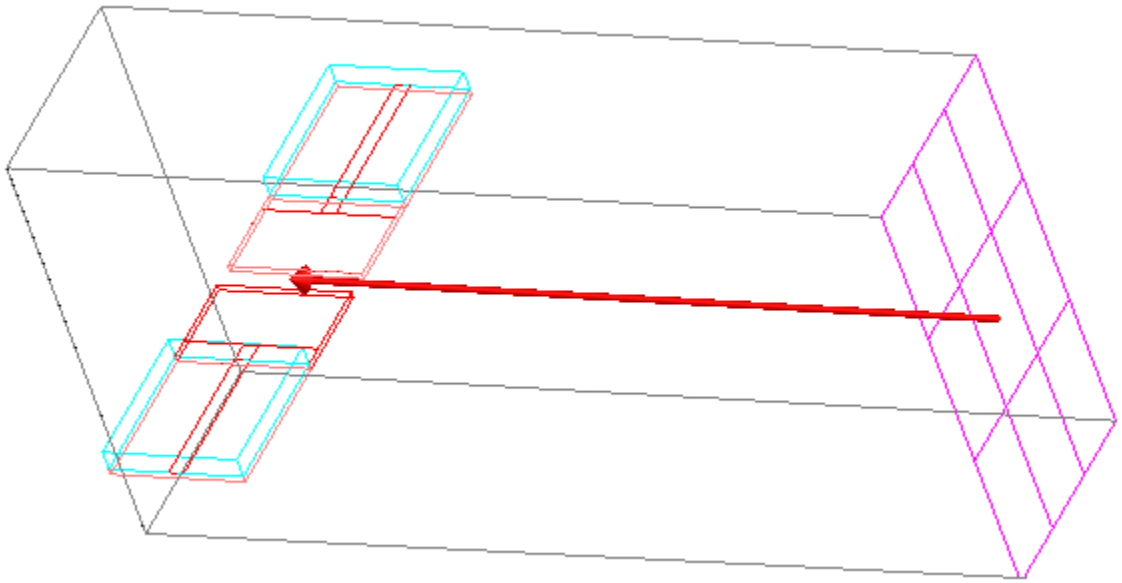

Figure 5.6 Admittance seen at the end of the arrow.

Since HFSS provides the S parameters at the specified location, a simple MATLAB routine was needed to obtain the desired admittance. As the reflection coefficient was given by S_{11}, we can write

$$y_{cp} = \frac{1 - S_{11}}{1 + S_{11}},$$

where S_{11} is the complex reflection coefficient. On the other hand, equation (5.3) states that

$$y_{cp} = 2[g_p - jb_p + j\ \mathrm{cotan}(\phi_1)],$$

So that finally we obtain

$$\begin{cases} g_p = \dfrac{1}{2} real\{\dfrac{1-S_{11}}{1+S_{11}}\} \\ b_p = \dfrac{1}{2} imag\{\dfrac{1-S_{11}}{1+S_{11}}\} + \dfrac{1}{2}\mathrm{cotan}(\phi_1) \end{cases} \qquad (5.4)$$

Table 5.3 shows the design values compared with the simulated results.

DESIGN VALUES		SIMULATION RESULTS	
g_p	b_p	g_p	b_p
1.40	0	1.42	0.01

Table 5.3 Actual vs. Simulated results.

The values obtained from equation (5.4) were in good agreement with the ones chosen at the beginning of the design. The correspondence between the desired and simulated values of the probe admittance and the excellent functioning of the 4 way combiner / divider, strengthens our past assumptions and theory developed in chapters 3 and 4. The 15 dB return loss bandwidth obtained from Figure 5.4 is approximately 23%, whereas the 0.5 dB insertion loss was observed to be around 26 %.

Equivalent Circuit Approach

Using the equivalent circuit proposed in chapter 3, a contour plot that shows how the bandwidth changes with probe admittance was obtained, and could be used to see the optimized values of g_p and b_p so as to achieve broadband performance. As mentioned before, an equivalent circuit model approach was proposed. The schematic diagram of the circuit is given in Figure 5.7. The model was simulated using *Agilent's Advanced Design System* (ADS).

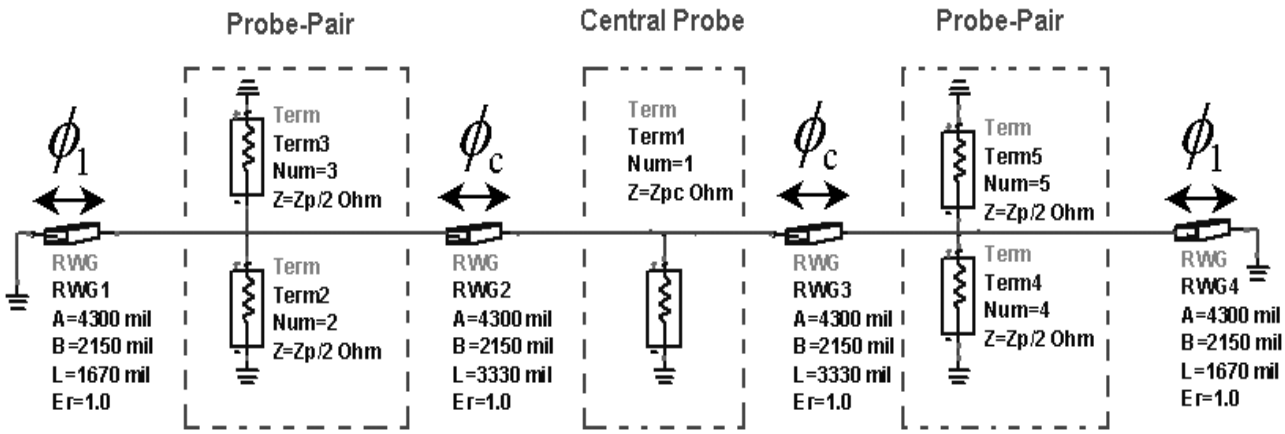

Figure 5.7 The equivalent circuit of the combiner /divider.

In the circuit, each section of waveguide is modeled by the corresponding rectangular waveguide (RWG) element in ADS, and the "Term" element is used to represent each individual probe. Thus we have a total of five "Terms". The width of the waveguide was given by A while its height was given by B, as clearly shown in

Figure 5.7. The central probe and the pair probe admittances, denoted as Z_p and Z_{pc}, respectively, were found by curve fitting the full-wave simulation results. These two parameters are frequency dependent and normalized to the waveguide impedance given by

$$Z_{PV} = \frac{377}{\sqrt{1-(\frac{1.372.10^9}{frequency})^2}}.$$

The equivalent circuit model represents the expected behavior of the system based on a transmission line analysis. From a circuit point of view, the probe impedance was halved in Figure 5.7 since the probe-pair had a parallel combination fed to the waveguide.

The scattering (S) parameters are plotted in Figure 5.8. Figure 5.8 displays the outcome obtained for the structure from ADS (refer to Figure 5.1 for port designations). These results agree well with HFSS through the entire R band, with the insertion loss exhibiting the expected value of approximately 6 dB. The 15 dB return loss was found to be approximately 23%. No asymmetry is to be found in the insertion loss results of Figure 5.8, as the central probe is represented by a simple admittance and wave propagation is modeled using standard transmission line analysis and not field theory.

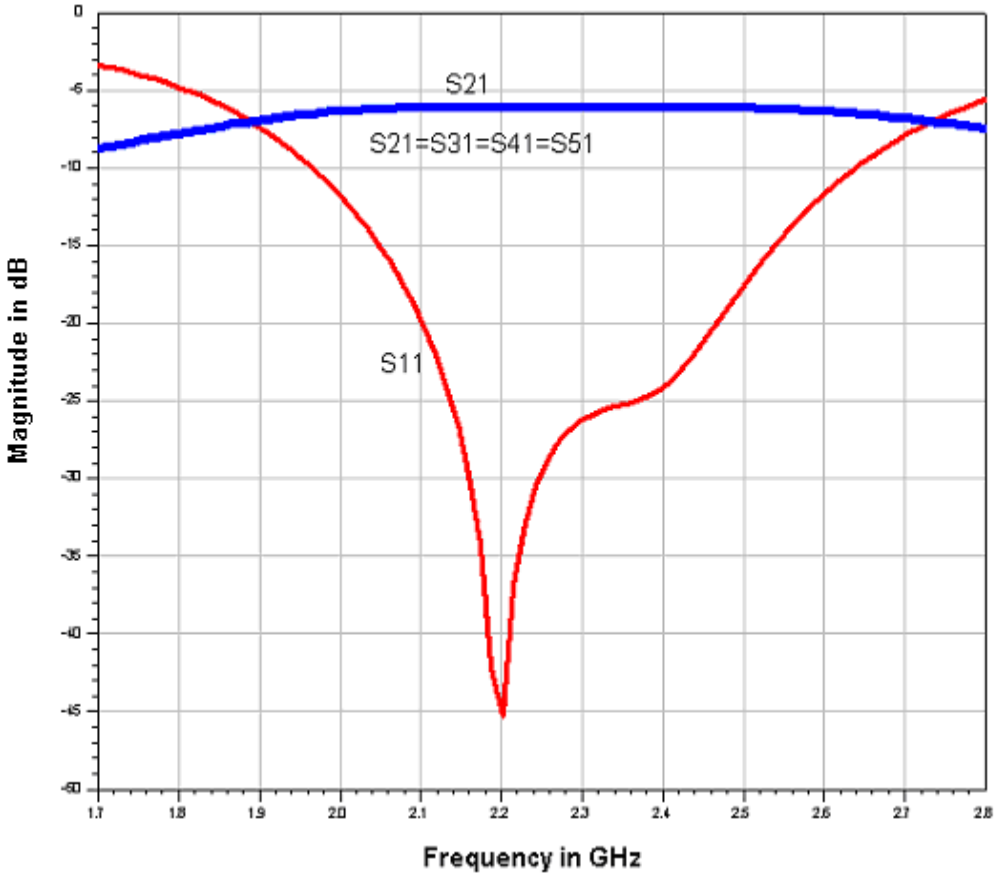

Figure 5.8 (S) parameters given by ADS.

A contour plot was generated from the equivalent circuit model, since it was easier to adjust b_p and g_p independently. Figure 5.9 shows the result of such an exercise.

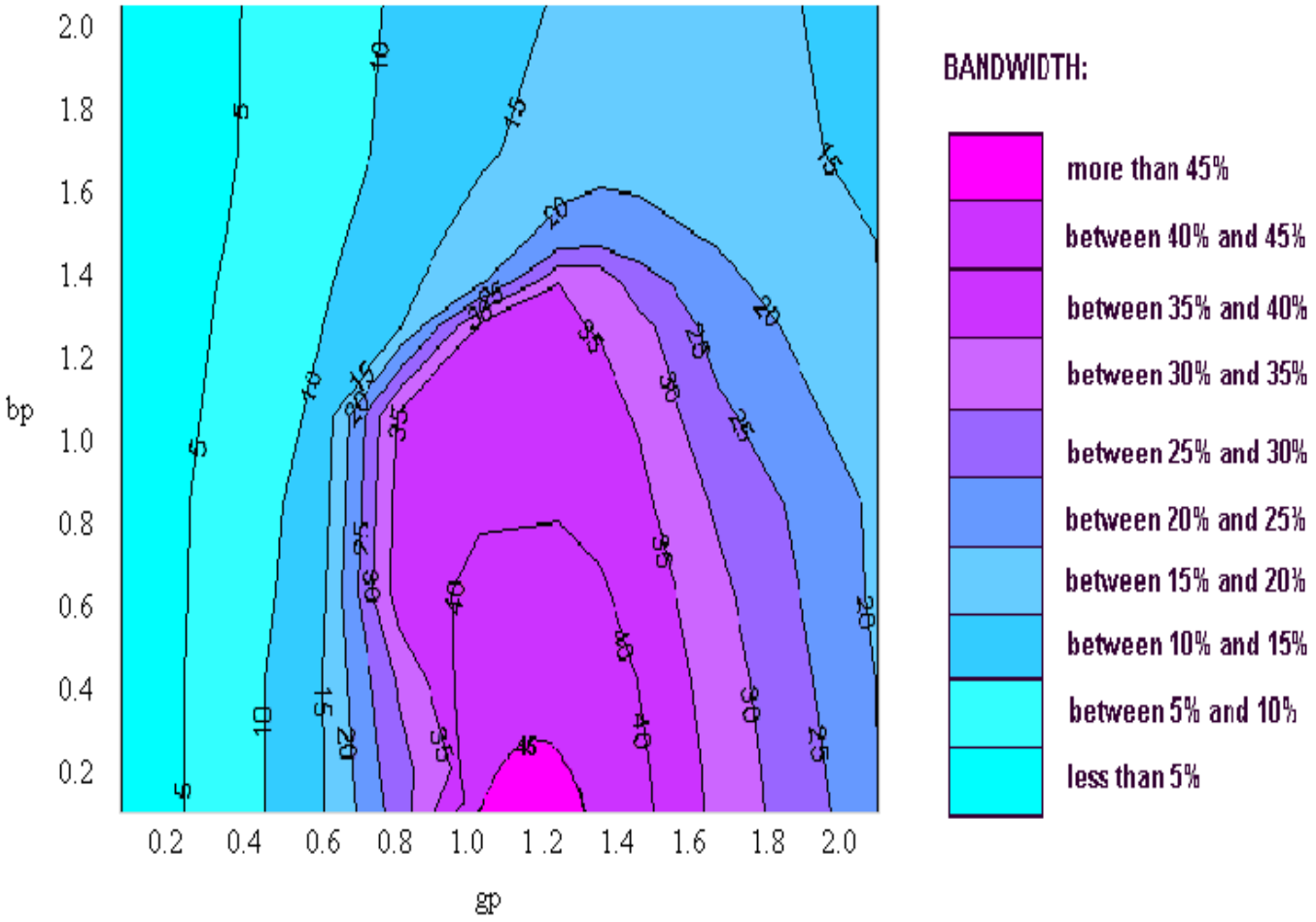

Figure 5.9 Contour plot of the combiner /divider.

From Figure 5.9 we see that the 0.5 dB bandwidth is between 40% and 45%. The reason for not obtaining the widest bandwidth possible is that we assumed b_p and g_p were frequency independents, while in fact they do depend on frequency.

Building the Structure

The microstrip double ladder waveguide was built in a rectangular block split along the E-plane of the dominant TE mode. Small channels were also realized at the bottom half to accommodate the probes. The bottom half of the aluminum-machined structure is shown in Figure 5.10. The WR-430 combiner / divider was measured in the microwave lab with a two-port vector network analyzer (VNA). A SOLT[8] calibration technique was needed before measurements were to be made. All measurements were referred at the end of the cables connecting the VNA to the divider, while the other three remaining ports of the waveguide were terminated by 50 Ω coaxial matched loads.

The structure could also be realizable via micromachining processes, as demonstrated in [4] and [5], where a split block waveguide and an E-plane probe were realized using bulk micromachining techniques. Such structures have been implemented using either a combination of wet anisotropic etching, and/or deep reactive ion etching and utilized finite ground coplanar lines for the probe feed [4].

[8] SOLT calibration: Short Open Load Through.

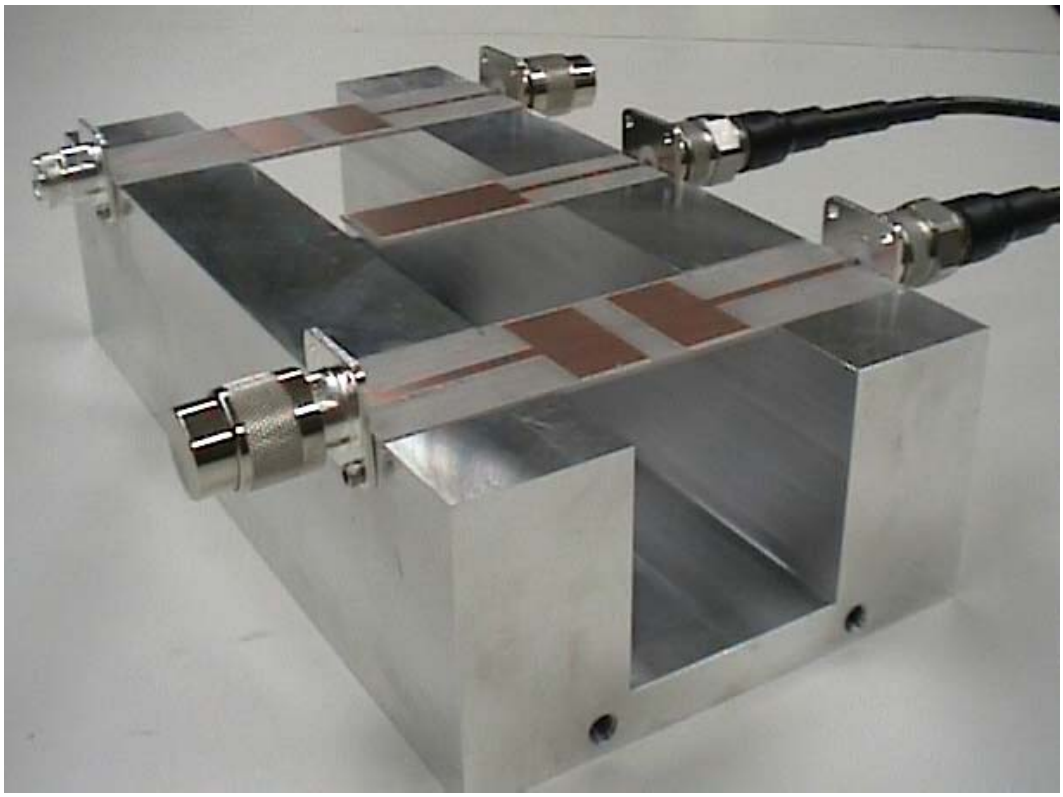

Figure 5.10 Photograph of the bottom half of the double ladder divider / combiner.

The results obtained from the VNA were imported to MATLAB [13] and printed as shown in Figure 5.10. It is evident from Figure 5.11 that the S parameters agree well with both the full-wave simulation and the ADS results. Note that the best match was not exactly at the desired frequency of 2.24 GHz; however, the general behavior (insertion loss, reflection loss…etc) of the frequency response agrees well with the predicted outcome, which is clearly apparent in Figure 5.12.

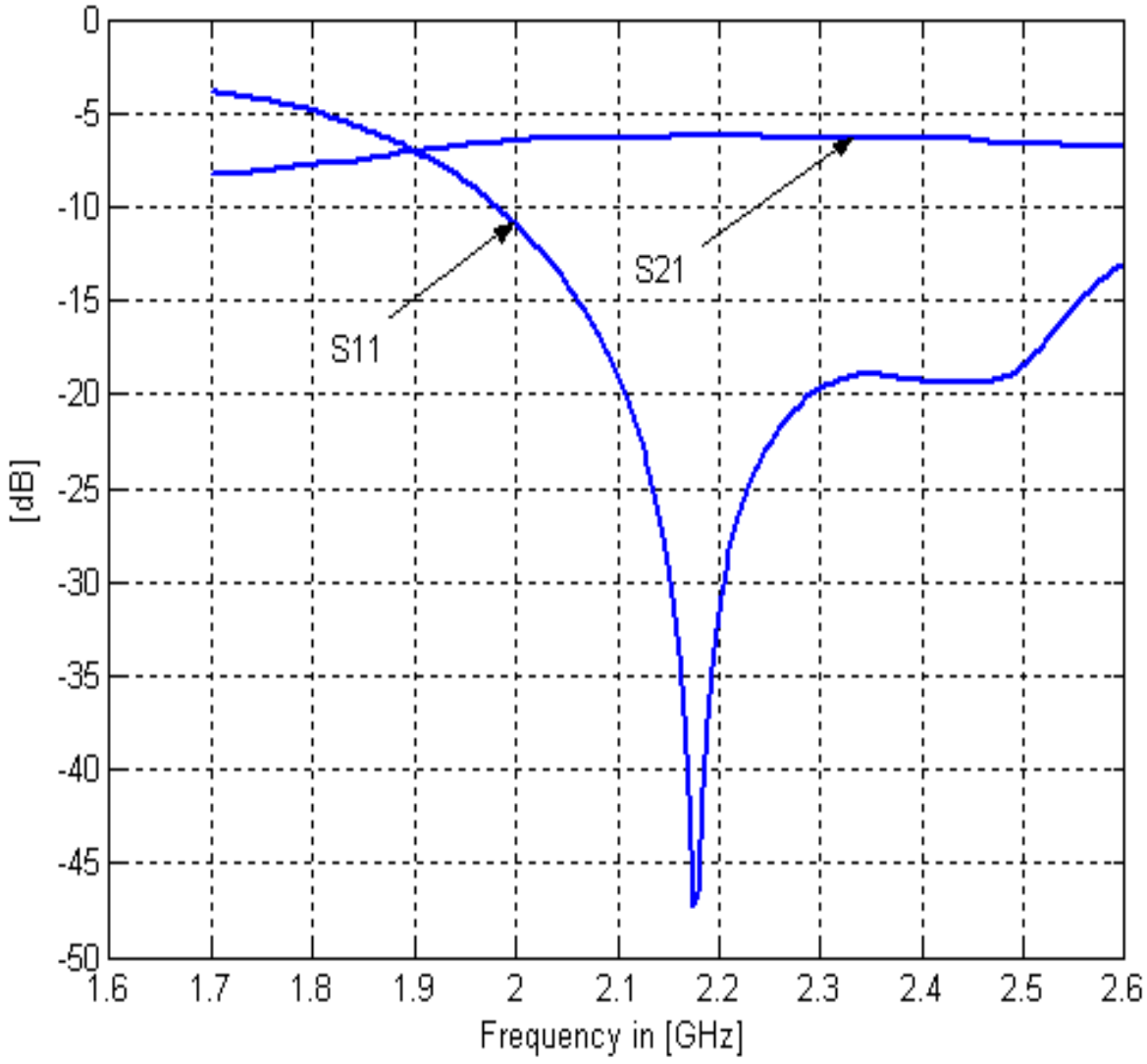

Figure 5.11 The S parameters of the machined waveguide.

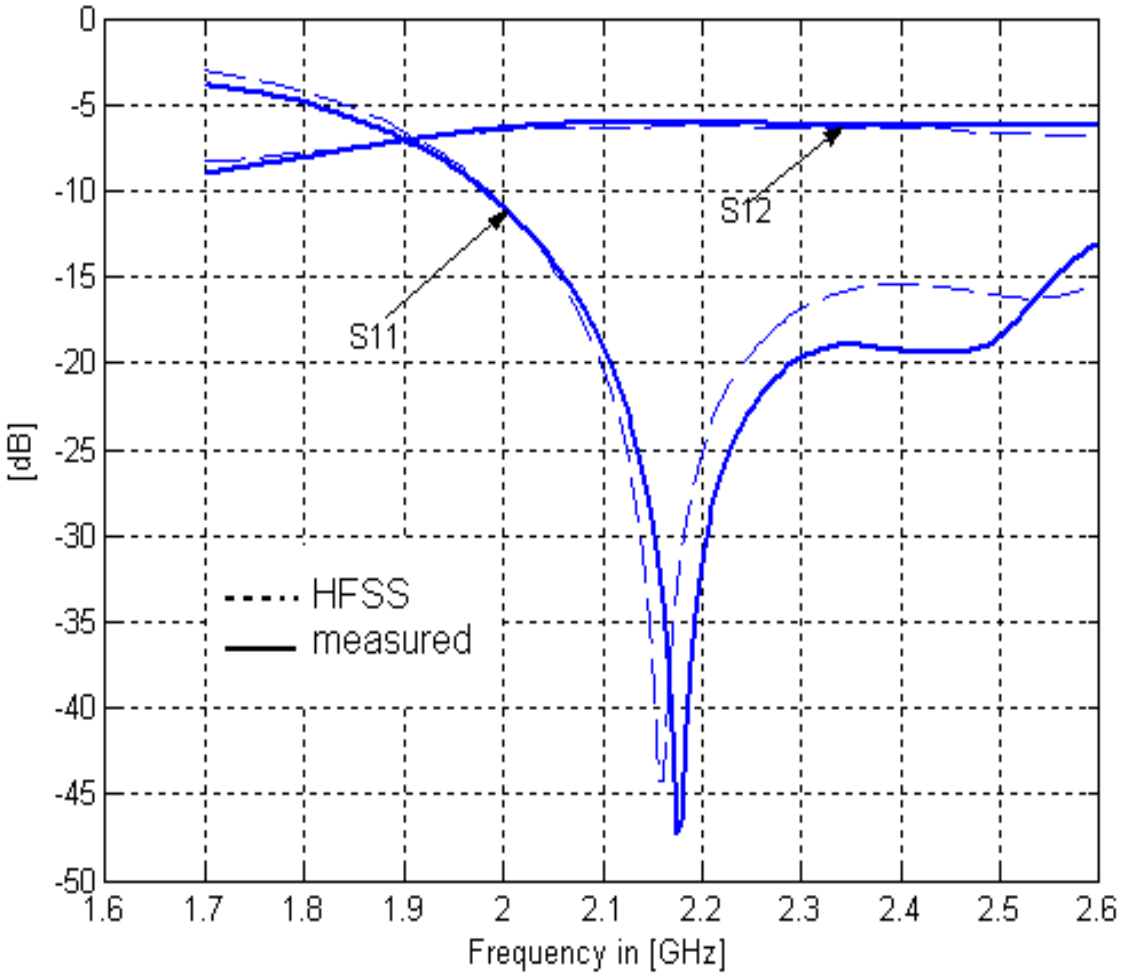

Figure 5.12 Comparing HFSS simulation to measured data..

The slight difference between the predicted performance and the actual one can be because the probe conductances used in the equivalent circuit were obtained by de-embedding in HFSS, where we assumed that there was no substrate existing in the waveguide. Overall, the results of this investigation suggest that the theory developed and the equivalent circuit model approach provide good design tools.

CHAPTER SIX

CONCLUSION

This thesis presents the initial steps towards developing waveguide-based power combining structures suitable for operation at W-band and above. The design equations which describe the equivalent circuit of a candidate for such power combining applications were derived, and verify the work of Sanada et al.[6].

Sanada et al. investigated the so-called coaxial double ladder power combiner. This structure relies on a series of coaxial fed probes to inject power into a waveguide cavity. Such a structure acts equally well as a power divider. While the coaxial double ladder structure may be used at microwave frequencies, realizing such a structure at millimeter and submillimeter wave frequencies is cost prohibitive. To satisfy the need for cost-effective power combining structures that operate at W-band and above, the planar probe double ladder structure has been considered. Using a combination of equivalent circuit modeling and full-wave simulation, a scaled model of a 4-way planar probe double ladder power combiner / divider has been designed. The structure was realized using conventional machining techniques and demonstrated in R band. Comparison of expected, simulated and measured results for R band showed good qualitative and quantitative agreement. The combiner exhibited a 15 dB return loss bandwidth of approximately 22% and a 0.5 dB insertion loss bandwidth of roughly 26%.

The structure was designed in such a manner that it could be realized using proven micromachining techniques for low-cost implementation at W-band and above. The demonstrated 4-way planar probe waveguide-based power combiner / divider was not optimized. For example, the probe admittances that were selected were not the optimal values. Rather, the values chosen were the best values possible, based on an existing waveguide block (i.e. L_1 and L_c were fixed). Additionally, the realized admittance values (as determined through full wave simulation) were close to, but not precisely equal to the desired admittances. Finally, the design was based on the assumption of frequency independent probe admittance. A design which intelligently considers the true frequency behavior of probe admittances would likely allow for a somewhat improved bandwidth[9]. The coplanar combiner could be improved through tuning several crucial parameters, one of which is achieved by placing the design frequency at a lower value within the waveguide's band, assuring that operation is well below the appearance of unwanted modes.

The planar combiner / divider exhibited up to a 0.25 dB difference in insertion loss between probes. We believe this asymmetry in response can be corrected by multiple techniques. One promising means is to increase the distance between the central probe and the inner probe pairs (i.e L_c). Doing so will presumably allow the wave emanating from the central port to assume a symmetric TE10 mode. This means of resolving the

[9] Improved by few percent

insertion loss asymmetry will result in a decrease in bandwidth which in some applications may be unacceptable. As shown in Figure 6.1 we can introduce an iris [17] to modify the field in the proximity of the central probe in hopes of correcting field asymmetry.

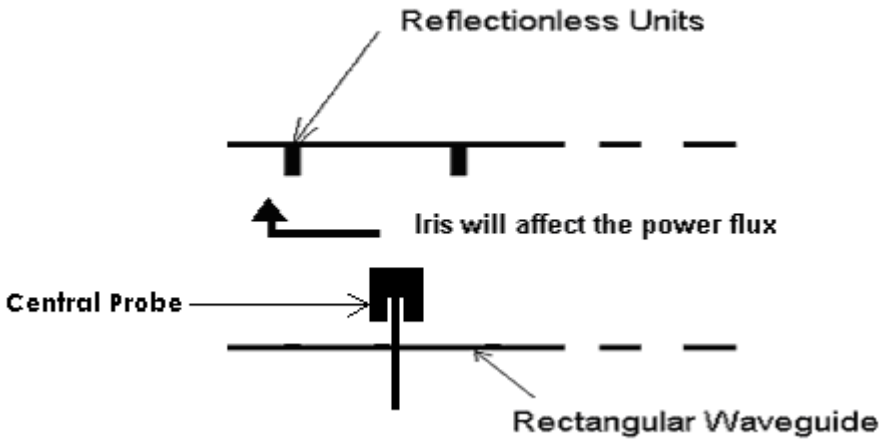

Figure 6.1 Top view of the waveguide divided by small reflection-less irises.

The current work has set the foundation for a broad-based examination of micromachined compatible waveguide power combiners / dividers. Important future work includes: improvement in the symmetry of electrical performance, examination of the structures performance for $N \geq 2$, and experimental demonstration of a fully micromachined version.

REFERENCES CITED

[1] Youngwoo Kwon, Dimitris Pavlidis, Timothy L. Brock and Dwight C. Streit, "A D-band Monolithic Fundamental Oscillator Using InP-Based HEMT's" IEEE Transactions on Microwave Theory and Techniques, Vol 41, No. 12, pp. 2336-2344, December 1993.

[2] H. Eisele, "Two-terminal devices as fundamental solid-state terahertz oscillators," in Terahertz Spectroscopy and Applications II, SPIE Proceedings Vol. 3829, pp.70-80, 1999.

[3] Kai Chang, Cheng Sun, "Millimeter-Wave Power-Combining Techniques" IEEE Transactions on Microwave Theory and Techniques, Vol. MTT-31, No.2, pp.91-107, February 1983.

[4] James P. Becker, Yongshik Lee, Jack R. East, Linda P. B. Katehi, "A finite Ground Coplanar Line-to-Silicon Micromachined Waveguide Transition," IEEE Transactions on Microwave Theory and Techniques, Vol. 49, No.10, pp.1671-1676, October 2001.

[5] James P. Becker, Yongshik Lee, Jack R. East, Linda P. B. Katehi, "A Micromachined Finite Coplanar Line-to-Silicon Micromachined Waveguide Transition For Millimeter and Submillimeter Wave Applications," IEEE MTT-S Digest.

[6] Atsushi Sanada, Kiyoshi Fukui, Shigeji Nogi, "A Waveguide Type Power Divider / Combiner of Double-Ladder Multiple-Port Structure," IEEE Transactions on Microwave Theory and Techniques, Vol.42, No 7, pp. 1154-1161, July 1994.

[7] High Frequency Structure Simulator from Ansoft, Version 4.1.00

[8] Chris Wayne Hicks, *Experimental and Electromagnetic Modeling of Waveguide-Based Spatial Power Combining Systems,* PhD thesis, North Carolina State University, 2002

[9] Pengcheng Jia, *Broadband High Power Amplifiers Using Spatial Power Combining Technique,* PhD thesis, University of California Santa Barbara, December 2002.

[10] Robert A. York, "Some Considerations for Optimal Efficiency and Low Noise in Large Power Combiners," IEEE Transactions on Microwave Theory and Techniques, Vol. 49, pp.1477-1482, August 2001.

[11] David B. Rutledge, Nai-Shuo Cheng, Robert A. York, Robert M. Weikel II, and Michael P. DeLisio "Failures in power-combining arrays," IEEE Transactions on Microwave Theory and Techniques, Vol. MTT-47, pp. 1077.1082, July 1999.

[12] A.A.M. Saleh, “Improving the graceful degradation performance of combined power amplifiers,” IEEE Transactions on Microwave Theory and Techniques, Vol. 28, pp. 1068-1070, October 1980.

[13] http://www.fnrf.science.cmu.ac.th/theory/waveguide/Waveguide%20theory%209.html

[14] K. Fukui, S. Nogi, S.Oishi, and A. Sanada, “Ladder Type Microwave Power Divider / Combiner’s,” Trans. IEICE Japan, Vol. J74-C-I, no. 1, pp27-37, Jan. 1991

[15] Advanced Design System from Agilent, Version 2003A

[16] MATLAB, Version 6.5.0

[17] Atsushi Sanada, Kiyoshi Fukui, Shigeji Nogi, Minoru Sanagi “Traveling-Wave Microwave Power Divider Composed of Reflectionless Dividing Units,” IEEE Transactions on Microwave Theory and Techniques, Vol.43, No 1, pp. 14-20, January 1995.